

Measurements and Computations of Natural Transition on the NASA Juncture-Flow Model with a Symmetric Wing

Andrew N. Leidy*, Michael A. Kegerise†, Judith A. Hannon‡, Meelan M. Choudhari§

NASA Langley Research Center, Hampton, VA 23681

Balaji Shankar Venkatachari¶, Pedro Paredes||

National Institute of Aerospace, Hampton, VA 23666

Experiments were performed in the 14- by 22-Foot Subsonic Tunnel to assess natural transition on the symmetric-airfoil wings of the NASA Juncture-Flow Model. Infrared thermography was used to visualize the heating on the upper surface of both wings of the full-span model, and on the fuselage, for angles of incidence ranging from -10° to 10° at a fixed Reynolds number of 2.4×10^6 based on the chord length at the wing planform break. The fuselage boundary layer transitioned well upstream of the wing-root leading edge for all conditions. Transition fronts were identified by a steep rise in the surface temperature, and the transition coordinates were transformed from an image-based to a body-fixed system. Additionally, the state of the boundary layer was estimated at pressure ports distributed on the wings through observation of the pressure coefficient as a function of the angle of incidence. For increasing angles of incidence, the transition front was observed to advance upstream, in a mostly spanwise-uniform fashion, from near midchord at $\alpha = 0^\circ$; however, for increasingly negative angles of incidence, the transition front first receded and then advanced in a nonuniform jagged manner that is typically observed with stationary crossflow. The transition wedges first appeared inboard of the wing break and then spread outboard to near the tip by $\alpha = -6^\circ$. The upstream shift in transition at positive angles of incidence and the outboard progression of crossflow-dominated transition at increasingly negative angles of incidence are consistent with trends identified in a computational assessment of the boundary-layer transition based on both linear stability analysis and Reynolds-averaged-Navier-Stokes-based transition models. The stability results obtained from the Langley Stability and Transition Analysis Code were used to recalibrate a dual N -factor criterion, which allowed for the prediction of transition fronts that showed excellent agreement with the experiment. The Reynolds-averaged-Navier-Stokes-based models, from the NASA OVERFLOW 2.3 solver, that accounted for the crossflow instability showed mixed results in comparison with the experiment, with the helicity-based Langtry-Menter model performing the best. The experimental data, particularly the cases involving strong influence from both Tollmien-Schlichting and crossflow instabilities, will be valuable for the continued validation and improvement of transition models.

Nomenclature

| | |
|-----------|---|
| c | local chord length |
| c_b | chord length at wing planform break, 580.716 mm |
| C_p | surface pressure coefficient |
| h_ξ | streamwise metric factor |
| h_ζ | spanwise metric factor |
| I | intensity, counts |
| M | Mach number |
| N | logarithmic amplification factor |

*Research Aerospace Engineer, Flow Physics and Control Branch, M.S. 170, Member AIAA.

†Research Scientist, Flow Physics and Control Branch, M.S. 170, Member AIAA.

‡Aerospace Engineer, Flow Physics and Control Branch, M.S. 170, Member AIAA.

§Research Scientist, Computational AeroSciences Branch, Associate Fellow AIAA.

¶Sr. Research Engineer, Computational AeroSciences Branch, Senior Member AIAA.

||Sr. Research Engineer, Computational AeroSciences Branch, Senior Member AIAA.

| | |
|----------------------|--|
| $\bar{\mathbf{q}}$ | vector of base flow variables |
| $\hat{\mathbf{q}}$ | vector of perturbation variables |
| $\hat{\mathbf{q}}$ | vector of amplitude variables |
| Q | dynamic pressure, Pa |
| R_a | roughness average, μm |
| Re_{cb} | Reynolds number based on chord length at wing planform break |
| R_q | roughness rms, μm |
| s_i | (s_1, s_2, s_3) Cartesian coordinates for camera calibration, mm |
| t | time, s |
| T | temperature, K |
| T_a | ambient temperature, K |
| (u, v, w) | streamwise, wall-normal, and spanwise velocity, $\text{m}\cdot\text{s}^{-1}$ |
| U_{ref} | reference velocity, m/s |
| x | body-fixed streamwise coordinate, mm |
| x_{LE} | body-fixed streamwise coordinate from local wing leading edge, mm |
| y | body-fixed spanwise coordinate, mm |
| y^+ | near wall grid spacing in wall units |
| z | body-fixed height coordinate, mm |
| α | angle of incidence, deg |
| $\hat{\alpha}$ | streamwise wavenumber, m^{-1} |
| β | spanwise wavenumber, m^{-1} |
| κ_ξ | streamwise curvature, m^{-1} |
| κ_ζ | spanwise curvature, m^{-1} |
| λ | spanwise wavelength, mm |
| ω | disturbance angular frequency, $\text{rad}\cdot\text{s}^{-1}$ |
| ρ | density, $\text{kg}\cdot\text{m}^{-3}$ |
| σ | spatial growth rate, m^{-1} |
| (ξ, η, ζ) | streamwise, wall-normal, and spanwise coordinates, m |

I. Introduction

THE NASA Juncture-Flow experimental effort consists of several ground-test entries with the primary goal of producing validation data of the flow at the trailing edge of the wing-fuselage junction. Experimental data near the junction is particularly valuable due to high levels of computational uncertainty in predicting separation distances and Reynolds stresses in that region.¹ The data collected from the series of NASA Juncture-Flow entries will provide for the improvement of turbulence models in predicting separated corner flows. Two previous campaigns were conducted in the NASA Langley 14- by 22-Foot Subsonic Tunnel using wings based on the DLR-F6 configuration.²⁻⁵ Several diagnostic tools were utilized to study the flowfield at the trailing-edge junction. Unsteady pressure measurements and oil flow visualizations determined the extent of the separated region. On-board laser doppler velocimetry (LDV)⁴ and particle image velocimetry (PIV)⁵ systems, stowed within the model fuselage, measured the velocity components and Reynolds stresses in planes near and upstream of the junction region. Surface pressure measurements were made at ports distributed across the model. The state of the incoming boundary layer was assessed using shear stress sensors and IR thermography. Away from the model, mean static pressure measurements were made on the ceiling, the port-side wall, and the starboard-side wall of the test section. The mean total pressures were also acquired from a set of boundary-layer rakes mounted to the ceiling, the port-side wall, and the starboard-side wall. Additional information about the Juncture-Flow tests, the dataset, and related publications can be found on the NASA TMR website.⁶

The present test entry aspires to repeat many of those diagnostics techniques, while replacing the DLR-F6 wings with symmetric-airfoil wings. Increased emphasis is placed on the detection of the natural transition front, utilizing IR thermography and surface pressure measurements. The natural transition measurements are the topic of this paper and were conducted prior to the juncture-flow measurements. A separate paper⁷ focuses on LDV measurements made near the trailing edge juncture.

IR thermography has become a preferred method for determining the state of the boundary layer due to its global and nonintrusive nature and the resolution that can be achieved. The transition front can be readily observed using IR due to the difference in convective heat transfer rates to the surface beneath laminar and turbulent boundary layers.⁸

IR thermography has been used extensively for boundary-layer transition detection in flight and ground tests. The best results are obtained on surfaces that have a high emissivity and low thermal conductivity. These material properties work to minimize reflections and maintain sharp features.⁹

The main objective of the transition portion of the present test entry was to determine how the transition mechanisms and nature of the transition front change with angle of incidence. Preliminary stability computations were run by Venkatachari et al.¹⁰ in preparation for the present test entry. They predicted that the Tollmien-Schlichting (TS) instability would be the dominant transition mechanism at positive angles of incidence, and stationary crossflow (CF), particularly inboard on the wing, would progressively have more of an influence at increasingly negative angles of incidence. These findings are consistent with the experimental results of Dagenhart and Saric,¹¹ who tested a swept wing with a NASA NLF(2)-0415 airfoil and observed the transition mechanism shift from TS- to CF-dominated as the angle of incidence decreased from 4° to -4°.

Venkatachari et al.¹⁰ also used Reynolds-averaged Navier-Stokes (RANS)-based transition modeling to predict the position of the transition front for selected angles of incidence. A more detailed quantitative assessment of the transition fronts is made herein, using a variety of RANS-based transition models and stability-based methods. Increased focus is placed on the angles of incidence where the transition front is influenced by both TS and CF mechanisms. The experimental results presented herein provide a well-characterized dataset that will be used to help improve the transition models.

Section II describes the tunnel and model geometry for the present test entry. The experimental methods are presented in section III, followed by the numerical methods in section IV. The experimental and numerical results are both presented in sections V and VI, respectively. Section VII gives a discussion of the results, and section VIII closes out the paper with some conclusions.

II. Test-Entry Details

This section introduces the testing facility and the model used in the present campaign.

A. 14x22 wind tunnel

The NASA Langley 14- by 22-Foot Subsonic Tunnel (14x22) is a closed-circuit, atmospheric-pressure wind tunnel capable of operating in open, partially closed, or closed test-section modes. Measurements for this study were made in the closed test section mode, where the test section measures approximately 4.42 m high by 6.63 m wide by 13 m long.

Throughout the campaign, the chord Reynolds number, Re_{cb} , was held at a constant value of 2.4×10^6 to within ±0.30%. Since the facility has no temperature control, the freestream velocity was adjusted to maintain a constant Re_{cb} as the air temperature changed over the course of a run and from day-to-day due to viscous heating and changes in the outdoor conditions. The nominal test conditions and their associated ranges for this test entry are shown in Table 1.

The freestream turbulence intensity was recorded by Neuhart and McGinley¹² as between 0.07 and 0.08% at a dynamic pressure of 2.87 kPa at the test section center height, 87 in. (2.2 m) above the floor. The turbulence intensity was roughly 20% higher at an elevation of 51 in. (1.3 m), which was closer to the position of the wing leading edges at the most negative angles of incidence in the present campaign. The reason for the difference in model elevation is explained in the next section. Additional details about the 14x22 tunnel can be found in Gentry et al.¹³

Table 1. Nominal test conditions and associated ranges.

| | Nominal value | Range |
|-----------------|------------------|---------------|
| Re_{cb} | $2.4 \cdot 10^6$ | ±0.30% |
| M | 0.189 | 0.174 – 0.192 |
| T_a , K | 288.84 | 282 – 300 |
| U_{ref} , m/s | 64.4 | 58.4 – 66.6 |
| Q , Pa | 2385 | 2115 – 2530 |

B. Juncture-flow model

The Juncture-Flow Model is a full-span wing-fuselage body that can be configured with different fuselage nose sections and different wing designs. Each wing design has a removable leading-edge insert at the root that allows the wing to be configured with or without a fairing to mitigate the leading-edge horseshoe vortex of the wing-fuselage junction. For the present study, the juncture-flow model was configured with the shorter of two available fuselage nose sections and symmetric wings with leading-edge root fairings. Top and side views of the model are shown in Fig. 1. The symmetric wing design is a blending of an NACA 0015 section at the root, an NACA 0012 section near the Yehudi break, and an NACA 0010 section further outboard, meaning that the wing thickness decreases due to both the changing airfoil and decreasing chord length across the span. The wing has a leading-edge sweep angle of 37.3° and a planform break located 869.7 mm from the model centerline. The planform break chord length, c_b , is 580.716 mm and serves as the reference length for Re_{c_b} . The overall length, height and width of the fuselage for this configuration is 4.838 m, 0.630 m, and 0.472 m, respectively, and the tip-to-tip wingspan is 3.327 m. The model was attached, by a long sting cannon, to a motorized sting mast that allowed for adjustments to the model pitch and yaw angles, as well as the model height.

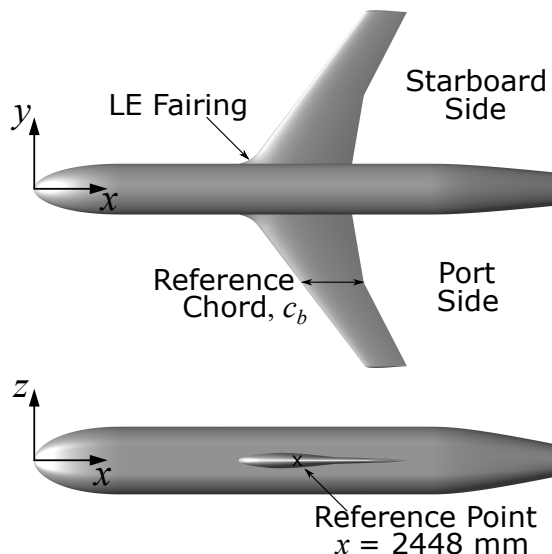


Figure 1. Top and side views of the Juncture-Flow Model.

The model was painted with a black lusterless polyurethane paint suitable for infrared imaging. The paint thickness was on the order of 254 to 330 μm , and the final layer was not sanded to maximize the emissivity. The high emissivity allowed for measurement of IR radiation representative of the model surface rather than reflected sources like the wind-tunnel walls or ceiling. Roughness measurements were taken on both painted wings prior to and during the test entry. The starboard wing consistently measured slightly rougher than the port wing. The average roughness, R_a , on the starboard side was $2.869 \pm 0.013 \mu\text{m}$, and the rms roughness, R_q , was $3.532 \pm 0.015 \mu\text{m}$. The respective measurements on the port side were $2.512 \pm 0.014 \mu\text{m}$ and $3.104 \pm 0.016 \mu\text{m}$. The spectra were broad and did not show any distinct peaks. Details on the roughness measurements and spectral content are reported in Ref. 14. A few isolated paint bumps were eliminated by spot sanding at the beginning of the campaign to prevent turbulent wedges from originating near the leading edge.

The model nose was located roughly 2.96 m downstream of the test section entrance and centered on the tunnel width. The height adjustment allowed for a reference point on the model (located at $x = 2448$ and $z = 0$) to be kept near the center of the test section, at a nominal elevation of 87.0 in. (2.21 m) above the test section floor, during a pitch-angle adjustment. However, the model height was progressively adjusted downward at increasingly negative angles of incidence due to sting-mast length limitations. The height of the reference point dropped for $\alpha < -3^\circ$, and the elevation was only 53.6 in. (1.36 m) at $\alpha = -10^\circ$. Additionally, the sting cannon was motorized for adjustments to the model roll angle. Both the pitch and roll angles were measured with a pair of accelerometer-based model-attitude sensors located inside the model fuselage. The roll angle was never intentionally adjusted but did show a roughly linear relationship with the angle of incidence, ranging from approximately -0.07° at $\alpha = 10^\circ$ to 0.07° at $\alpha = -10^\circ$.

III. Experimental Methods

This section explains the methods used to prepare for the test and to collect and process the experimental data.

A. Infrared measurement preparation

1. Camera calibration

Three 1344 x 784 resolution midwave (3–5 μm) infrared (IR) cameras were used to image the transition front on the port and starboard wings and on the port side of the fuselage nose. All cameras were fitted with 25 mm, $f/4.0$ lenses for a wide field of view. Camera calibrations were obtained prior to testing to correct for perspective distortion. The calibrations were accomplished by imaging a custom IR grid. Incandescent bulbs from a string of “Christmas lights” were inserted through holes in a fiberglass-laminate plate (G10). The lights were arranged in a 9 x 6 grid with 4 in. (101.6 mm) spacing. The IR grid worked well since the bulbs were easily distinguished from the nonthermally-conductive backing. Calibrations were performed at different distances to bound the anticipated camera-to-model distances during the test entry. The calibrations were done in one-foot (305 mm) increments, ranging from 7 to 10 ft. (2.13 to 3.05 m) for the two cameras allocated for the wings, and 10 to 12 ft. (3.05 to 3.66 m) for the camera imaging the nose. More than twenty images were taken at each distance, with the target physically positioned in at least three different orientations and the camera tilted at various angles to place the target at different positions within the field of view.

The camera calibrations were determined through the following process. The light bulb positions were identified in each image by evaluating the centroid location for each bulb. These “image points” were sorted for all images, with the same bulbs arranged in the same order. A corresponding “world point” grid was also generated by setting one corner of the physical IR grid as an origin and then defining a 2-D grid according to the theoretical dimensions of the IR grid. Matching these physical points to those identified in the images allowed for estimates of the intrinsic and extrinsic parameters and the distortion coefficients of the camera. A representation of the extrinsic parameters for a calibration performed at a distance of 8 ft. (2.44 m) is given in Fig. 2. This figure shows the twenty-two different positions of the IR grid relative to the camera when the images were taken.

The discrepancies were minimal between the calibrations obtained at different distances. The 7 and 10 ft. (2.13 and 3.05 m) camera calibrations were applied to a representative $\alpha = 0^\circ$ port-wing image. The difference between the transition fronts was evaluated, and the rms value of the difference in the x -transition coordinates across the span was only 0.65 mm. The calibrations obtained at distances of 8 ft. (2.44 m) and 10 ft. (3.05 m) were applied to the wing cameras and the fuselage nose camera, respectively, since those were approximately the distances encountered during the test entry.

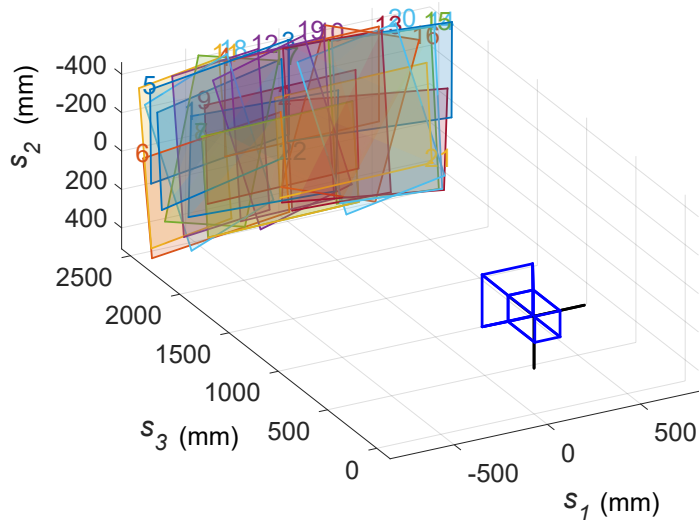


Figure 2. Visualization of the extrinsic parameters. Twenty-two positions of the grid are shown in physical space relative to the camera.

2. Fiducial markers

Fiducial markers were placed on the model to map the 2-D calibrated IR images into body-fixed coordinates. The markers were retroreflective, with a low emissivity in comparison to the wings. They were thin ($20\pm5\text{ }\mu\text{m}$ thick) and placed a sufficient distance downstream of the leading edge to prevent disturbance of the flow. The markers had a diameter of 10 mm, which was large enough for identification in the images and to calculate a centroid. Eight markers were affixed to each wing and two additional markers were placed on the fuselage above each wing to increase the physical depth. Seven additional markers were placed farther upstream on the port side of the fuselage for the nose images. The position of each marker, in body-fixed coordinates, was measured using an 8-axis portable coordinate measuring machine. The base of the machine was positioned in three locations to reach the three measurement regions. An overlapping marker was measured with the nose markers and the port wing markers to confirm that the measured coordinates were consistent. At each region, at least eight known locations of static pressure ports were first measured to obtain reference coordinates. The position of each marker was measured by defining three points around the perimeter of the marker and, separately, by measuring the marker center. The 2-sigma uncertainty for any fiducial marker coordinate is 1.24 mm. The largest uncertainty values are generally in the coordinate that is nearly normal to the surface.

B. Data acquisition

1. IR thermography

The IR camera dedicated to the port side of the fuselage nose viewed the model through an open port in the north wall. The IR cameras for the wings viewed the model through separate ports in the ceiling. The cameras were each fastened to a ball-head rotational element that was secured to an extruded-aluminum rail, which allowed each ceiling camera to image nearly the entire wing in its field of view for all angles of incidence. All three IR cameras acquired data once the tunnel was on condition and the model reached the desired angle of incidence. One-hundred frames were taken at each point, with a typical exposure time of 15 ms. This exposure was chosen to maximize the dynamic range of the 14-bit detector. Vibrational motion during the sampling at each point was subpixel in magnitude. The nose camera was levelly mounted for a couple of runs and then was pitched downward for a run to capture the negative angle-of-incidence cases below $\alpha = -2.5^\circ$ since the model height in tunnel was lower for those points. A transition front was resolved for 21 points, including at least one point for each angle of incidence between $\alpha = -10^\circ$ and $\alpha = 10^\circ$, inclusive, in 2.5° increments. Trip dots were added to the nose following those three runs, while additional IR images were taken on the wings. The nose trip dots did not impact the transition front on the wings.

Transition data were collected on the wings over the course of twelve runs on five different days. The orientation of both cameras mounted above the ceiling did not appreciably change during this time. The transition front was resolved for 188 and 157 points on the port and starboard wings, respectively. The angles of incidence encompassed $\alpha = -10^\circ$ to $\alpha = 10^\circ$, in both 2.5° and 1° increments. Finer, 0.25° , increments were taken between $\alpha = -6^\circ$ and $\alpha = -2^\circ$.

The outdoor weather had a large influence on the quality of the IR images since there was no heating mechanism within the wings. The ideal weather for these tests involved cool mornings, with overnight lows between 0°C and 5°C , that warmed up to above 10°C with sunshine throughout the day. For consistent images, it was important to have turbulent heating rates be higher than laminar rates and for the fiducial marks to appear cold relative to the model wall. To facilitate these trends, the model and the wind tunnel walls were “cold soaked” overnight, meaning the test section doors to the 14x22 circuit were left open to allow the model and walls to cool far below room temperature. This step minimized the time at the start of every run where the laminar and turbulent heating trends were inverted from the norm, resulting from the flow being colder than the model surface. Typically, the fiducial markers also appeared inverted, i.e., relatively hot, at the start of each run since the markers reflected the temperature of the tunnel ceiling. The tunnel ceiling was initially warmer than the model due to its location within the building but became relatively colder sometime during each run. It took up to 30 min for that reversal to happen when overnight lows were below 0°C . As a run progressed, the temperature difference decreased between the model and the flow, which reduced the contrast between the laminar and turbulent regions and worsened the quality of the images. The duration of acceptable laminar to turbulent contrast was extended with increasing outdoor temperatures and sunshine on the tunnel circuit. Those uncontrollable external conditions allowed the flow temperature to continually increase at a high rate ($> 0.002^\circ\text{C/s}$), which helped to maintain the temperature difference between the flow and model.

2. Surface pressure

The Juncture-Flow Model was instrumented with 244 static pressure ports on the fuselage and 289 static pressure ports on the symmetric wings. The inner diameter of each pressure port was 597–648 μm . Electronically scanned pressure (ESP) modules, which were stowed in the model fuselage and wings, measured the mean pressure at each port. The full-scale range of the modules was 1 psid (6.89 kPa) or 5 psid (34.47 kPa), depending on the expected pressure range of the ports connected to the module, and the modules were referenced to the ambient pressure in the control room of the 14x22 tunnel. Two sets of runs were conducted with full angle-of-incidence sweeps from $\alpha = -10^\circ$ to $\alpha = 10^\circ$ in 0.25° increments.

C. Transition detection

1. IR image processing

The following method was used to process the images from each camera at each test point. The one-hundred frames were averaged, and any noisy pixels were filtered through outlier detection. The resulting image was corrected for distortion using the appropriate camera calibration. The locations of all fiducial markers visible in the image were identified by finding the centroid of each marker. The location of the camera in body-fixed coordinates was then estimated based on the camera calibration, the image fiducial marker locations, and the body-fixed fiducial marker locations as measured by the 8-axis portable coordinate measuring machine. Knowing the location of the camera and the camera calibration parameters allows for the mapping of a 2-D IR image onto 3-D body-fixed coordinates.

Next, a surface mesh was generated for each image, with goals of encompassing the transition front and maintaining regular spacing, so all fronts at the same α could be easily compared. The x coordinate ranged from $x = 2150$ mm to $x = 3472$ mm on both the port and starboard wings. The x increment in the grid varied with angle of incidence but was always between 1–2 mm. The y -coordinate range depended on the position of the transition front. It was generally bounded between $y = \pm 440$ mm and $y = \pm 1640$ mm, with a fixed increment of 0.5 mm. The fuselage-nose z values were bounded from around $z = 300$ mm to $z = -300$ mm, and the x -coordinate values generally ranged from $x = 400$ mm to $x = 1000$ mm, with both coordinates resolved to 1 mm. The undefined coordinate, z for the wings and y for the fuselage nose, was determined through interpolation of the known geometry.

The intensity values, I , were then projected onto the mesh points. For the wings, the mesh was divided into streamwise slices, i.e., slices of constant y . The intensity values along each slice were evaluated in terms of streamwise distance (x). The derivative of the curve ($\partial I / \partial x$) was approximated using a central difference scheme, and the x locations of the top three derivative values were recorded as potential transition locations. With the transition potential defined across the entire wing, an initial transition location was established near the wing root by defining a starting point. From there, progress was made outboard to the next streamwise slice, with the primary potential location, i.e., the location with the highest derivative value, taking precedence, followed by the second or third choices. The location was only accepted as part of the transition front if the difference in x value from the previous location was within a threshold value. If none of the three points fell within the threshold, that y was skipped. The threshold value varied with angle of incidence since the nature of the transition front changed. Lower threshold values were used with angles of incidence that produced flat transition fronts compared to those that produced turbulent wedges. Certain obstacles, like the fiducial markers and the internal frame, had to be avoided to prevent deviation in defining the transition front. This was done by adjusting the mesh to avoid certain ranges of y values.

Similar steps were taken to locate the transition front on the fuselage nose. Derivatives of intensity were again obtained along streamwise slices. The transition location was established at a point near the top of the fuselage, and the front was evaluated by moving down in z .

A sample IR image of the port wing for an $\alpha = -5^\circ$ case is assessed in Fig. 3. The image is annotated in Fig. 3(a) to identify features specific to the model that must be considered when interpreting the image. Regions with denser internal structure typically were colder on the surface due to cold soaking the model overnight. The eight fiducial markers are depicted as small dark dots. They reflected the temperature of the test-section ceiling, which was relatively colder than the model surface. The boundaries of the leading-edge fairing are also observed. During the test, the turbulent boundary layer from the fuselage relaminarized on the fairing, but the interface of the fairing and wing at the leading edge caused a turbulent wedge that was especially noticeable for $\alpha \geq -1^\circ$. Therefore, the transition front analysis was conducted outboard of that wedge. A discontinuity also appears in the image along the leading edge. The image suggests that there is an external seam, but the differences are within the structure. The leading edge is hollowed at locations along the span to allow for pressure taps, which resulted in a higher surface temperature than the rest of the span due to the cold soaking. The five streamwise-aligned rows of pressure taps are numbered on the image.

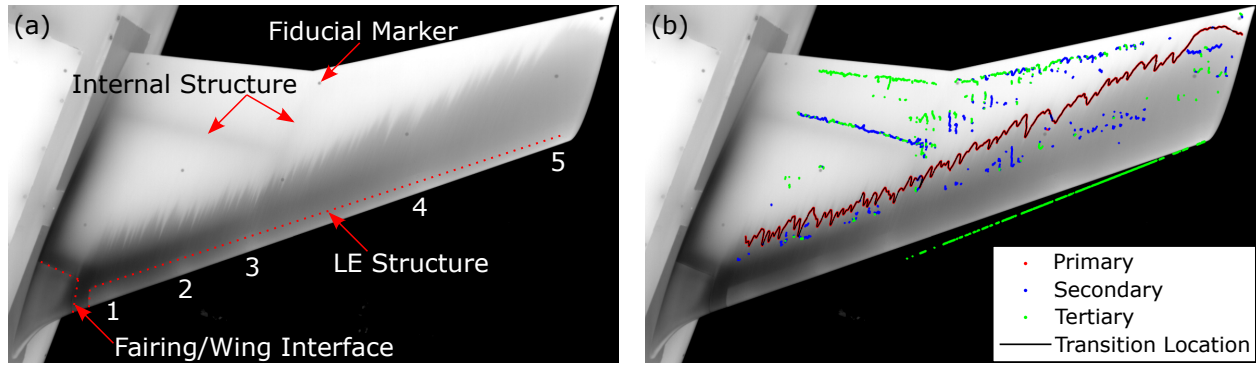


Figure 3. Sample IR image for an $\alpha = -5^\circ$ point. (a) IR anomalies particular to this test are annotated on the image. (b) Potential transition locations and the resulting transition front are plotted on the image.

The same image is shown in Fig. 3(b) overlaid by the map of potential transition locations marked as colored dots, with red as primary, blue as secondary, and green as tertiary. The transition front for this case is clearly defined by the primary potential locations. This is the direct result of an image with good contrast and was not always the case. The difference in temperature across the transition front for this particular point was $0.3 \pm 0.1^\circ\text{C}$. Secondary transition potential dots are seen here along the model internal structure and fiducial markers. The transition front would tend to divert to those features with images having less contrast between the laminar and turbulent regions, necessitating grid adjustments to keep the transition front on its correct course.

There are a couple of perspectives regarding the uncertainty in the location of the transition front on the wings. The first perspective is that uncertainty should include all factors related to the experiment, and the transition fronts on both wings should be considered together since they should, theoretically, be in the same position mirrored across the fuselage. In that case, flow nonuniformity and geometric and surface finish differences contribute to variations in the transition fronts between the two wings. Also included are the uncertainties accrued by adhering to a second perspective, which considers the results obtained on each wing separately. Uncertainties from that perspective are only based on factors related to the imaging and processing and the random errors associated with differences observed at the same angle of incidence. The uncertainty arising from the camera calibration are bounded by considering calibrations performed closer to and farther from the target than the measurements made during the actual test. The uncertainty based on the measurement of the fiducial markers using the coordinate measuring machine are estimated to a 2-sigma value. The uncertainty from the processing steps are limited to the step of rounding the location of maximum $(\partial I / \partial x)$ gradient to nearest 1–2 mm resolution of x grid since no pixel shifts occur in the image processing. Differences in transition fronts acquired at the same nominal angle of incidence are attributed to slight differences in α and random errors. The uncertainty due to random errors was reduced by acquiring more points at a given angle of incidence. Random errors are found to be lower for flat portions of the transition front compared to those that are turbulent-wedge dominated.

2. Surface pressure

The location of the transition front was estimated using the static pressure ports for angles of incidence between $\alpha = -2^\circ$ and $\alpha = 8^\circ$. The lack of spatial resolution near the leading edge above $\alpha = 8^\circ$, and the breaking of spanwise-uniform transition-front trends for $\alpha < -2^\circ$ prevented those estimates from being made. Four streamwise rows of pressure ports on each wing were considered for the transition detection analysis. The rows are at $y = \pm 482.6, 685.8, 869.7$, and 1295 mm.

The pretest analysis indicates an increase in static pressure as the flow transitions from laminar to turbulent.¹⁰ From previous, unpublished observations, Dr. Jenna Eppink suggested conducting angle-of-incidence sweeps in fine increments to estimate the transition location. The static pressure measurements were used to estimate the transition front based on the following process and illustrated in Fig. 4. The pressure coefficient (C_p) was plotted as a function of α at each pressure port. A sample plot for the port located at $(x, y) = (2920, -1295)$ mm is given in Fig. 4(a). The plot shows both sets of runs where the wing naturally transitioned, and the data show great repeatability. Also plotted for reference is a dataset where the entire upper wing surface was turbulent as a result of effective boundary layer tripping just downstream of the leading edge. A “hitch” is observed on the natural transition curves, centered at $\alpha = 3.625^\circ$, where the transition front passes over that specific port. The flow is turbulent over the port at higher

angles of incidence. The α at the central part of the hitch, the point between the ends of the laminar and turbulent curve trends, was estimated at each port to the nearest 0.125° . The x -location of each pressure port was plotted against the transition α for each row of ports, and a quadratic curve was fit through the points. This plot for all of the rows of ports considered herein is shown in Fig. 4(b). Obtaining a curve fit for each row allowed for a direct estimation of the x -transition location for a given α . The transition front at a given α was defined using line segments to connect the x -transition locations at the four rows of pressure ports on each wing.

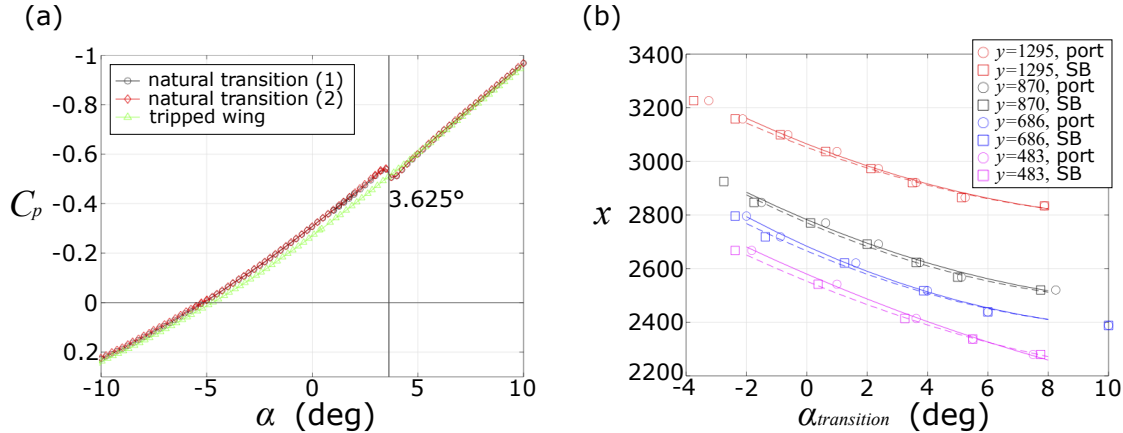


Figure 4. (a) A sample C_p vs. α curve for the pressure port at $(x, y) = (2920, -1295)$ mm. Boundary-layer transition occurs at $\alpha = 3.625^\circ$, where the “hitch” is observed. (b) Transitional α values plotted for each pressure port along the 4 rows of ports considered on the port and starboard (SB) wings. A quadratic curve was fit to the data to approximate the transition location for a given α .

IV. Numerical Methods

Contours of the pressure coefficient over the Juncture-Flow Model, and the C_p distribution at selected spanwise wing locations, for different angles of incidence, were previously reported by Venkatachari et al.¹⁰ Based on those data, it can be inferred that the flow undergoes rapid acceleration near the leading edge of the wing for positive angles of incidence. Downstream of the leading edge, for much of the wingspan, the flow encounters an adverse pressure gradient over the entire chord length that becomes stronger with increasing angle of incidence. A strong adverse pressure gradient over a long expanse leads to high growth of the TS boundary-layer instability. For negative angles of incidence, the pressure gradient is initially favorable from the leading edge. A minimum pressure is reached at increasing distances downstream for increasingly negative angles of incidence. A long region of favorable pressure gradient flow on a swept wing leads to high growth of the CF boundary-layer instability. Therefore, instability analysis of TS and CF and transition models associated with those instabilities are evaluated herein.

The NASA OVERFLOW 2.3b solver¹⁵ is an implicit Navier-Stokes solver for structured, overset grids that is capable of computing both time-accurate and steady-state solutions via a variety of options for spatial and temporal discretizations. This solver was used to obtain the mean-flow solutions that were implemented for performing the stability analysis and for computations involving RANS-based transition models. OVERFLOW was run in a steady-state manner by using the 3rd-order Roe upwind scheme,¹⁶ and the unfactored successive symmetric overrelaxation (SSOR) implicit solution algorithm.¹⁷ While the original model is full span, the computations were carried out for a semispan geometry under the assumption of symmetry across the x - z plane. The baseline mesh used in the previous work of Venkatachari et al.¹⁰ was also used here, as the adequacy of this mesh was confirmed by the grid convergence study reported therein. The mesh had seven overset near-body blocks (three on the fuselage, including on the nose and tail, one wing-body collar grid, and three on the wing, including the tip). The generation of off-body grids and hole cutting was carried out by using the OVERFLOW domain connectivity function (DCF) approach. The near-body grids surrounding the wing and fuselage had 325 points in the wall-normal direction with ten uniformly spaced points adjacent to the wall with a near-wall spacing of $2.6 \mu\text{m}$ ($y^+ = 0.5$), followed by a growth rate of 1.02. The near-body grid also contained 433 points around the wing in the chordwise direction (25 points on the trailing edge) and 463 points in the spanwise direction. The near-body grid had an overall grid count of approximately 140 million points. The far-field boundaries of the outer-body grids were placed at approximately $100c_b$. The computations assumed an adiabatic wall, model symmetry, and freestream boundary conditions.

The following subsections describe the computations used to evaluate boundary-layer transition over the symmetric wings of the NASA Juncture-Flow Model.

A. Stability analysis

The instability characteristics of wing boundary layers are conventionally examined by applying the local infinite-swept-wing assumption in order to study the evolution of instability waves along the chordwise direction, i.e., perpendicular to the leading edge. Under this assumption, the computational coordinates can be defined as an orthogonal body-fitted coordinate system, with (ξ, η, ζ) denoting the streamwise, wall-normal, and spanwise coordinates. Density and temperature are denoted by ρ and T . The metric factors are defined as

$$h_\xi = 1 + \kappa_\xi \eta, \quad (1)$$

$$h_\zeta = 1 + \kappa_\zeta \eta, \quad (2)$$

where κ_ξ and κ_ζ denote the streamwise and spanwise curvatures, respectively. The Cartesian coordinates are represented by (x, y, z) . The vector of fluid perturbation variables is $\tilde{\mathbf{q}}(\xi, \eta, \zeta, t) = (\tilde{\rho}, \tilde{u}, \tilde{v}, \tilde{w}, \tilde{T})^T$, the vector of amplitude functions is $\hat{\mathbf{q}}(\eta) = (\hat{\rho}, \hat{u}, \hat{v}, \hat{w}, \hat{T})^T$, and the vector of basic state variables is $\bar{\mathbf{q}}(\eta) = (\bar{\rho}, \bar{u}, \bar{v}, \bar{w}, \bar{T})^T$. The streamwise and spanwise wavenumbers are $\hat{\alpha}$ and β , respectively, and ω is the angular frequency of the perturbation. The spanwise wavelength is defined as $\lambda = 2\pi/\beta$.

Additionally, the stability characteristics of the 3-D boundary layer over the wing can also be studied with a nonorthogonal curvilinear coordinate system as implemented in the LASTRAC.3d code.¹⁸ The nonorthogonal curvilinear coordinate system allows for the streamwise direction to be along the streamline, while the spanwise direction is along the spanwise surface grid lines that run parallel to the leading and trailing edges. The remaining coordinate is in the wall normal direction. Results for boundary layers over infinite-swept-wing configurations have been shown to be identical between the orthogonal and nonorthogonal coordinate systems.¹⁸

The streamwise curvature and nonparallel effects are considered in the context of the parabolized stability equations (PSE). The PSE approximation is based on isolating the rapid phase variations in the streamwise direction. The effects of instability wave propagation within a fully 3-D boundary layer can also be evaluated by performing the parabolic integration along stream or group velocity lines. The perturbations have the following form

$$\tilde{\mathbf{q}}(\xi, \eta, \zeta, t) = \hat{\mathbf{q}}(\xi, \eta) \exp \left[i \left(\int_{\xi_0}^{\xi} \hat{\alpha}(\xi') d\xi' + \beta \zeta - \omega t \right) \right], \quad (3)$$

where the unknown, streamwise varying wavenumber $\hat{\alpha}(\xi)$ is determined in the course of the solution by imposing an additional constraint

$$\int_{\eta} \hat{\mathbf{q}}^H \frac{\partial \hat{\mathbf{q}}}{\partial \xi} h_\xi h_\zeta d\eta = 0, \quad (4)$$

which implies a slow variation of the amplitude functions $\hat{\mathbf{q}}(\xi, \eta, \zeta) = (\hat{\rho}, \hat{u}, \hat{v}, \hat{w}, \hat{T})^T$ in the streamwise direction in comparison with the phase term $\exp \left[i \int_{\xi_0}^{\xi} \hat{\alpha}(\xi') d\xi' \right]$. By substituting Eq. (3) into the linear Navier-Stokes equations and including the scale separation to neglect the viscous, streamwise derivative terms, the PSE are obtained in the following form

$$\left(\mathbf{L} + \mathbf{M} \frac{\partial}{\partial \xi} \right) \hat{\mathbf{q}}(\xi, \eta) = 0. \quad (5)$$

The entries of the coefficient matrices for \mathbf{L} and \mathbf{M} with a more detailed description of the method can be found in Refs. 18–20.

The nonparallel growth rate of the disturbance with a selected combination of ω and β is defined as

$$\sigma_{PSE}(\xi, \omega, \beta) = -\Im(\hat{\alpha}) + \frac{1}{2} \frac{dK}{d\xi}, \quad (6)$$

and is based on the disturbance Kinetic energy norm, K , calculated with

$$K(\xi) = \int_{\eta} \tilde{\mathbf{q}}(\xi, \eta)^H \mathbf{M}_K \tilde{\mathbf{q}}(\xi, \eta) h_\xi h_\zeta d\eta, \quad \mathbf{M}_K = \text{diag}[0, \bar{\rho}(\xi, \eta), \bar{\rho}(\xi, \eta), \bar{\rho}(\xi, \eta), 0]. \quad (7)$$

The onset of laminar-turbulent transition is estimated using the logarithmic amplification ratio, the so-called N -factor, relative to the neutral location ξ_I where the disturbance first becomes unstable,

$$N(\omega, \beta) = - \int_{\xi_I}^{\xi} \sigma(\xi', \omega, \beta) d\xi'. \quad (8)$$

Herein, we assume that transition onset is likely to occur when some threshold involving the combination of TS and CF N -factor envelope values is reached.²¹⁻²³ The expression of the dual $N_{TS} - N_{CF}$ criteria can be written as

$$\left(\frac{N_{TS}}{N_{TS,cr}} \right)^{a_{TS}} + \left(\frac{N_{CF}}{N_{CF,cr}} \right)^{a_{CF}} = 1, \quad (9)$$

where the subscript cr refers to the critical value, and the exponents a_{TS} and a_{CF} control the level of interaction between the two types of instability waves.

B. RANS-based transition models

The following RANS-based transition models available in the release version of OVERFLOW 2.3b were used herein: (i) the two-equation Langtry-Menter γ - $Re_{\theta t}$ transition model (LM2009)^{24,25} coupled with the year 2003 version of Menter's shear-stress transport (SST) RANS model,^{26,27} along with the modifications proposed by Langtry et al.²⁸ to account for CF-induced transition (LM2015); (ii) Coder's^{29,30} 2017b version of the amplification factor transport (AFT 2017b) equation-based model that uses the Spalart-Allmaras (SA) model;³¹ and (iii) the Medida-Baeder model,^{32,33} which is a reformulation of the LM2009 transition model to allow for its integration with the SA model.

Additionally, the extension of the Langtry-Menter model to include the local helicity-based CF model as proposed by Grabe et al.³⁴ was also implemented. This combination is designated henceforth as LM-CFHE. The AFT and Medida-Baeder models, as executed in OVERFLOW, only account for TS-induced transition and not for CF effects. As a result, those two models are not expected to give significantly different results from the LM2009 model. The results from the AFT model were documented previously by Venkatachari et al.¹⁰ Given the importance of CF effects in this campaign, the results from the LM2015 and LM-CFHE models are the primary focus, and the LM2009 model is used to help isolate the effects of the submodel for CF transition. According to the nomenclature of the NASA turbulence modeling resource,⁶ these transition models should ideally be referred to as LM2015/LM2009-CFHE/SST-2003-LM2009, respectively. However, for sake of brevity, they will be referred to as LM2015/LM-CFHE/LM2009 throughout this work.

V. Experimental Results

In this section, a summary of the experimental data is presented. The full set of IR transition data for the test entry will be available on the NASA TMR website in the near future.⁶

A. Sample IR images with features

Observations can be made regarding the nature of the transition fronts by examining select raw IR images of the port wing. Four representative images with different transition characteristics are shown in Fig. 5. The image representing the most negative angle of incidence, $\alpha = -10^\circ$, shows a transition front that is upstream of midchord for nearly the entire span. The nature of the transition front appears slightly different near the root compared to outboard of the break. The front is positioned slightly farther upstream near the root and also lacks the jaggedness that is observed outboard. For $\alpha = -3^\circ$, the transition front is farther downstream in comparison to $\alpha = -10^\circ$, but is jagged and advanced past midchord for the portion inboard of the break. Outboard, the front recedes downstream to nearly the trailing edge and is more uniform in appearance. For $\alpha = 3^\circ$, the front is upstream of midchord and mostly flat across the entire span with a few shallow advancements that can be mainly attributed to roughness near the leading edge due to pressure ports. At $\alpha = 10^\circ$, the transition front is very close to the leading edge and turbulent flow dominates the upper surface of the wing. A laminar separation bubble is observed near the leading edge in the form of a dark band that extends over the outer 2/3 of the wing. Wingtip effects also appear to be causing local cooling that extends from midchord to the trailing edge.

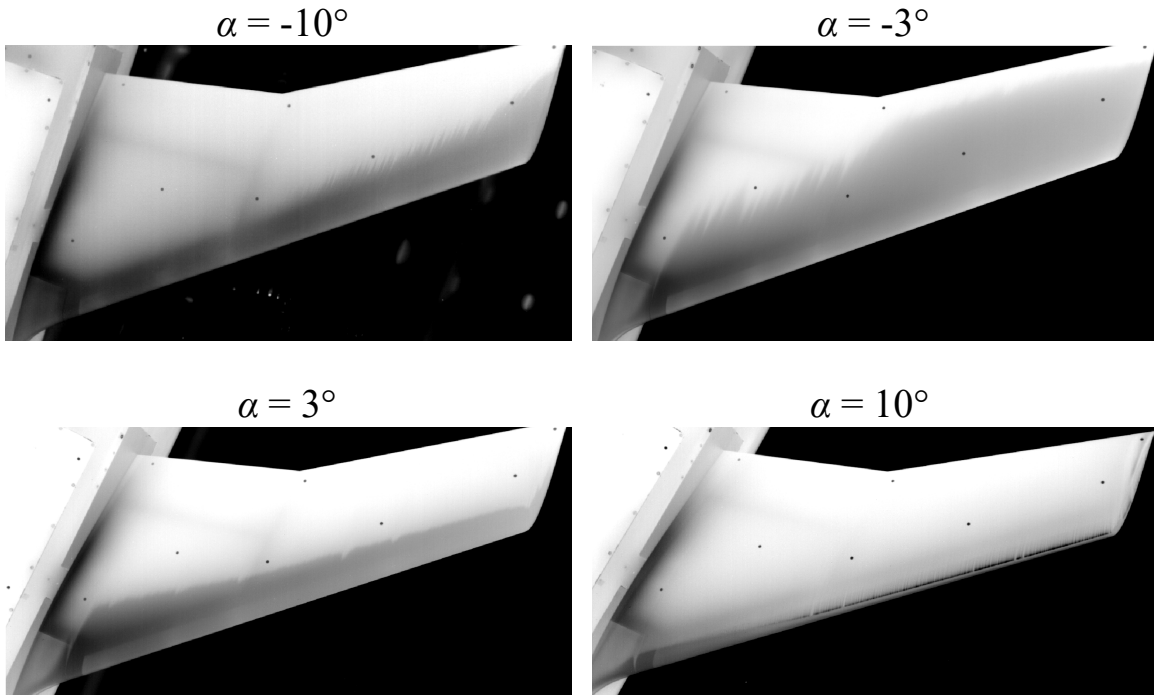


Figure 5. Sample IR images of the port wing for $\alpha = -10^\circ, -3^\circ, 3^\circ$, and 10° . These images are representative of the differences observed in the transition fronts over the tested α range.

B. Transition fronts from IR

The transition front was identified on all images following the methods outlined in Section III.C.1. A “median” x -transition coordinate was established by taking the median x -transition value for each y value across the span, using all points at a given angle of incidence. The median transition fronts on both the port and starboard wings for positive α , ranging from 0° to 10° , are shown in Fig. 6. The port and starboard fronts appear to be near reflections across the fuselage. As observed previously in Fig. 5, the front is near the LE across the span for $\alpha = 10^\circ$. Then it recedes downstream for every subsequent lower α and is near midchord across the entire span for $\alpha = 0^\circ$. The shape of the fronts are similar for all positive angles of incidence, in that they are all roughly parallel to the leading edge across the span, with just a few local upstream advances that are generally located at similar y values.

The median transition fronts for negative angles of incidence, ranging from -10° to 0° , are shown in Fig. 7. The transition fronts generally show good symmetry across the wings, but there is more variation at the less negative α . The transition fronts from negative α generally show more variability across the span in comparison to the positive α . Also, the behavior near the wing tip is significantly different compared to the positive α . The transition front for the positive cases either remains level or slightly advances, while the more negative cases, i.e., $\alpha < -5^\circ$, all trail off. Similar to the positive α mapping, the most extreme negative angle of incidence, $\alpha = -10^\circ$, gives the upstream-most transition front across the span. The transition front is mostly straight inboard of the wing break. Outboard, the variation in transition front location increases due to the turbulent wedges. There is significant overlap outboard of the break on both wings between the $\alpha = -10^\circ$ and $\alpha = -8^\circ$ cases, before $\alpha = -10^\circ$ extends farther across the span toward the wingtip. For $\alpha = -9^\circ$, not shown here, the straight portion is restricted to $y < 650$ mm. Angles of incidence $-8^\circ, -6^\circ$, and -5° show several crossings of each other on the inboard portion before separation is established between the fronts outboard. The transition fronts for $\alpha = -6^\circ$ and $\alpha = -5^\circ$ retreat the farthest downstream of any α near the wingtips, past $y = \pm 1600$ mm. For $\alpha > -6^\circ$, there is a change in the nature of the transition front. The front is advanced and jagged inboard of the break but then suddenly retreats at some outboard location and levels off far downstream. As α approaches -3° , the outboard flat portion of the transition front increases in span and advances incrementally upstream, while the jagged part is reduced in span and retreats downstream. By $\alpha = -2^\circ$, the turbulent wedges disappear, and the transition front looks similar to the positive angle-of-incidence cases. The entire front advances upstream as the α increases to 0° .

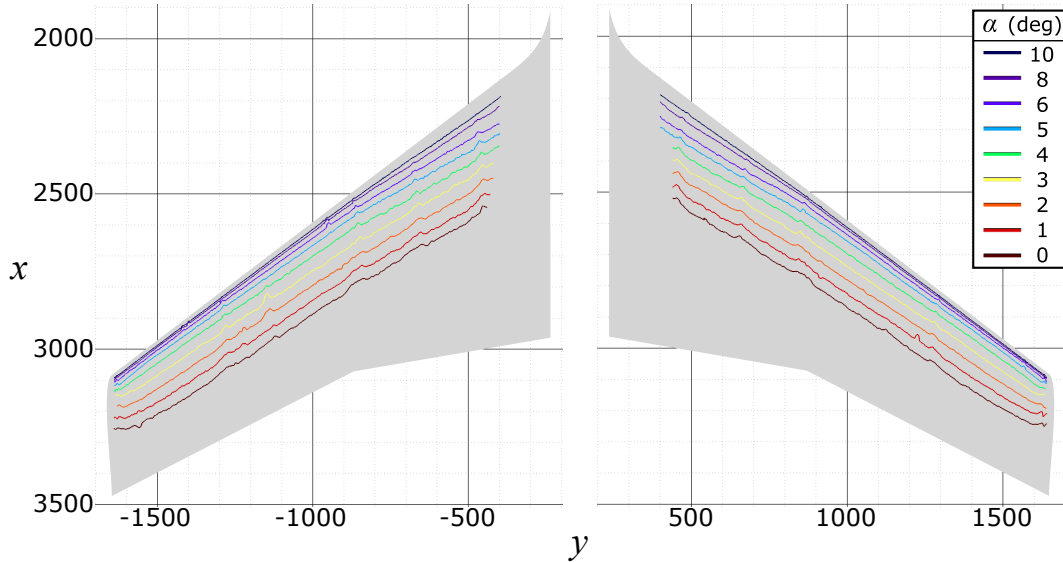


Figure 6. Transition fronts on both wings for positive angles of incidence, ranging from $\alpha = 0^\circ$ to $\alpha = 10^\circ$.

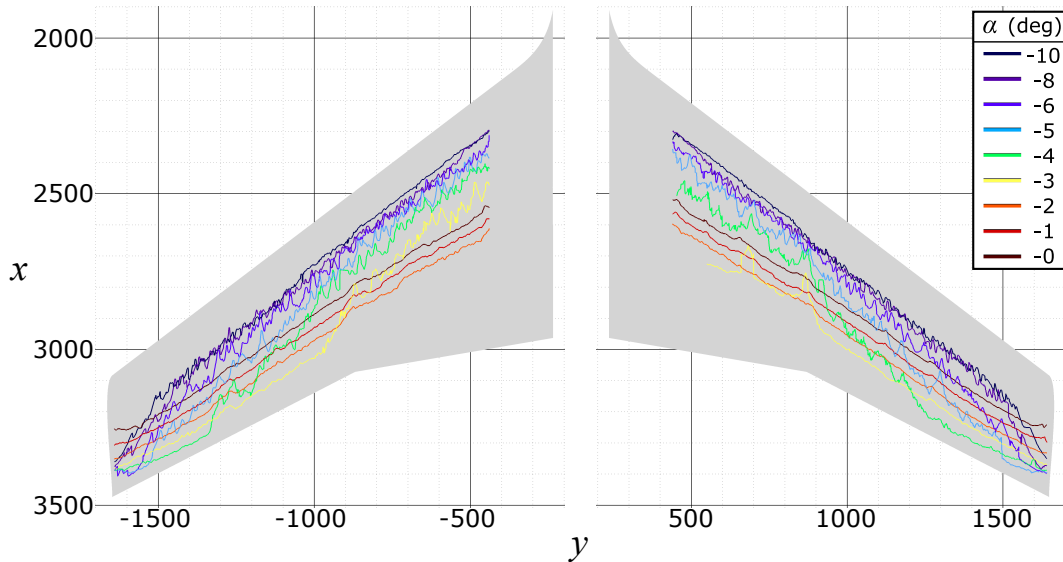


Figure 7. Transition fronts on both wings for negative angles of incidence, ranging from $\alpha = -10^\circ$ to $\alpha = 0^\circ$.

Figure 8 shows a smaller range of the more interesting negative α transition fronts. A couple of additional intermediate angles are included to further demonstrate the trends. The bounds of the α -values considered are -6° , characterized by a jagged front across the span and located mostly upstream of midchord, and -2° , which is generally flat and located entirely downstream of midchord. Within those bounds, similar trends are observed on both wings, but the absence of symmetry between the wings is most pronounced for this angle-of-incidence range. As α increases from -6° to -2° , the location on the span where the transition front significantly retreats progressively moves closer to the root, and the outboard receded portion increases in span. The port wing generally shows a wider span of turbulent wedges for the same α , and the inboard portion of the transition front is located farther upstream. For example, at $\alpha = -4^\circ$, the starboard wing transition front retreats to nearly the trailing edge by $y = 1250$ mm, while there is an advancement in the transition front at the corresponding spanwise location on the port wing. For $\alpha = -2.5^\circ$, the transition front is essentially flat on the starboard wing, but there is still a sizable span of jagged transition front advancement on the inboard portion of the port wing.

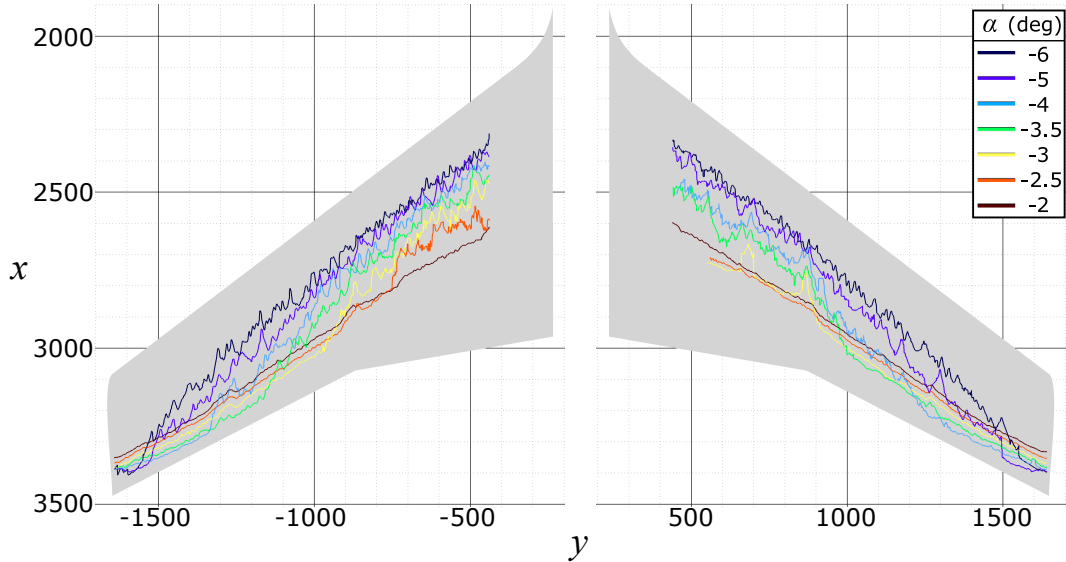


Figure 8. Transition fronts on both wings for negative angles of incidence between $\alpha = -6^\circ$ and $\alpha = -2^\circ$.

Comparisons are made between the transition fronts on the port and starboard wings in Fig. 9. The lighter dashed lines represent the transition fronts from the starboard wing, reflected over the fuselage and mapped on the port wing, while the darker shades are the corresponding fronts from the port wing. The agreement is strong between wings for $\alpha = -8^\circ$, with only slight deviations near the wing tip as the front recedes slightly more inboard on the port side. This strong agreement is also observed for the more extreme $\alpha < -8^\circ$ angles not shown here. The differences again are most pronounced for the intermediate negative angles of incidence, with $\alpha = -4^\circ$ shown here. The transition front is generally farther upstream inboard of the break on the port side. The front recedes downstream closer to the root on the starboard side, allowing for a longer span of the flat portion of the transition front. Although the span of that downstream segment of the transition front is longer on the starboard side, the port segment actually pushes farther downstream, closer to the trailing edge. Both transition fronts are relatively flat for $\alpha = -2^\circ$, with the starboard front farther upstream across the span.

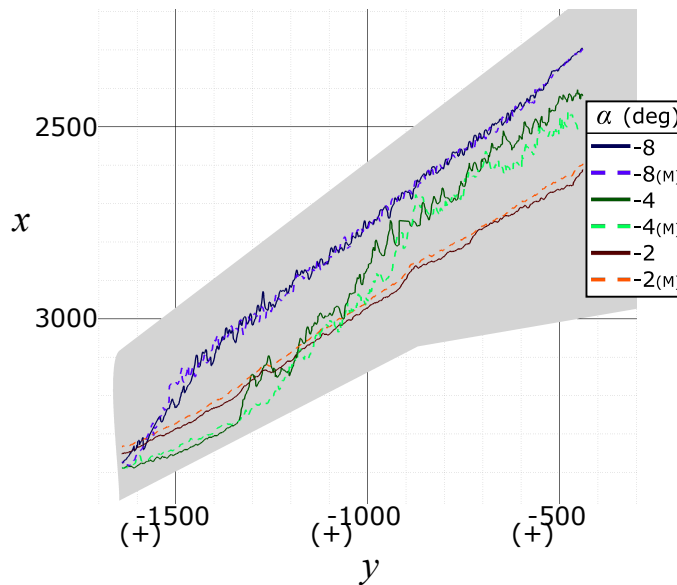


Figure 9. Transition fronts for $\alpha = -8^\circ$, -4° , and -2° . The transition fronts on the port side are shown as darker shades, while the transition fronts from the starboard side (M), mirrored over the fuselage and mapped on the port wing, are plotted as lighter dashed lines.

The transition-front repeatability is demonstrated in Fig. 10(a), where the minima and maxima x -transition values across the span are shown for two different angles of incidence on the port wing. Eleven points were considered for the $\alpha = -5^\circ$ case, which is a turbulent-wedge-dominated transition front. Despite the sizable number of points, there does not appear to be a substantial difference between the minimum and maximum cases, with most of the turbulent wedges in alignment. Even better agreement is observed for the $\alpha = 0^\circ$ case, where twenty-seven points were considered. Both the minimum and maximum curves show the same transition front shape with the same advances. The rms value of the difference between the minimum and maximum x -transition coordinates across the span was 19.76 mm and 7.08 mm for the $\alpha = -5^\circ$ and $\alpha = 0^\circ$ cases, respectively.

The transition location at the break, $y = \pm 869.7$ mm, as a function of angle of incidence is plotted in Fig. 10(b) for both wings. The transition location is specified as a fraction of chord length, and it was computed using the median transition front at each angle of incidence by taking the mean x -transition value between the bounds of $-864.5 \geq y \geq -874.5$ mm and $864.5 \leq y \leq 874.5$ mm for the port and starboard wings, respectively. The agreement in transition location at the break between the two wings is very good outside of the intermediate negative angles. This plot confirms some of the trends discussed previously. The transition front is farthest downstream at the wing break for $\alpha = -2.5^\circ$. As the angle of incidence becomes more negative, the front rapidly advances between $\alpha = -2.75^\circ$ and $\alpha = -4.5^\circ$, with the starboard side advancing earlier at the break despite the inboard features taking longer to appear. Both transition fronts continue to advance at a slower rate for $\alpha < -5^\circ$. There is a large amount of variability in slope, and even direction, on both curves between $\alpha = -3^\circ$ and $\alpha = -8^\circ$ due to the nature of the jagged transition front and the tendency of the turbulent wedges to shift with changing angle of incidence. The port wing is observed to transition farther upstream at the wing break for the most negative angle of incidence. A comparison with the transition fronts in Fig. 7 shows this to be more of a local phenomenon at the break since there is very good agreement over the rest of the span.

Moving from $\alpha = -2.5^\circ$ toward positive angles of incidence on Fig. 10(b), the starboard wing is observed to transition farther upstream as previously noted in the mirrored comparison (Fig. 9). Interestingly, the rate of transition front advancement from $\alpha = -2^\circ$ to $\alpha = 5^\circ$ is nearly a constant $0.07c_b$ on both wings. Note that this means the uncertainty in α alone would contribute to a $\pm 0.0014c_b = \pm 0.81$ mm uncertainty in the transition front location over this α range. By $\alpha = 5^\circ$ the transition front on both wings is within $0.15c_b$. Transition continues to advance at the higher angles but at a decreasing rate.

The difference between corresponding minima and maxima x -transition location values at the wing break (not shown here) is within $0.01c_b$ for most angles of incidence, with the largest difference of $0.052c_b$ for $\alpha = -5^\circ$ on the port side, which is the case shown in Fig. 10(a).

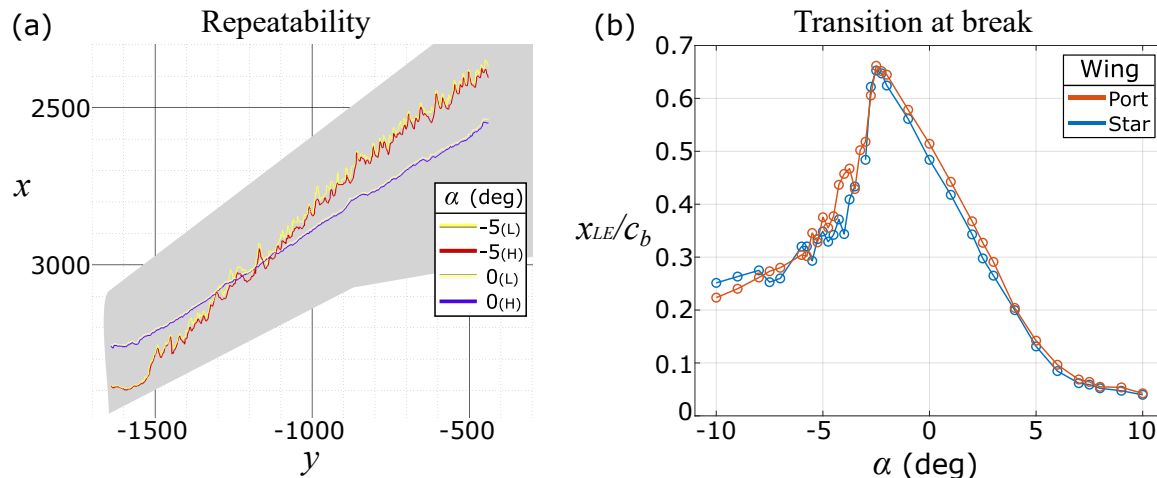


Figure 10. (a) Minima (L) and maxima (H) x -coordinate transition fronts for $\alpha = -5^\circ$ (11 points) and $\alpha = 0^\circ$ (27 points). (b) Streamwise location of the transition front at the wing break ($y = \pm 869.7$ mm) as a function of α .

The transition front on the port side of the fuselage nose for $\alpha = -10^\circ$ to $\alpha = -10^\circ$ is shown in Fig. 11. The positive angles of incidence are shown on the left, and the negative angles are on the right. The arrows indicate the respective flow directions at exaggerated angles and are directed toward the windward side of the nose. The $\alpha = 0^\circ$ case, which is shown in both images in green, demonstrates a transition front with some variation across the model

height. There are noticeable advancements around $z = \pm 120$ mm, which are due to the model geometry. The nose radius varies considerably, especially in the section where the nose evolves into a fuselage with flat side walls. The transition advancements align with increased nose curvature.

The $\alpha = \pm 2.5^\circ$ cases are similar to $\alpha = 0^\circ$, but with the leeward transition advancement shifted slightly away from the $z = 0$ and what appears to be a bifurcation of the original $\alpha = 0^\circ$ advancement, about its original height, on the windward side. The transition fronts for the $\alpha = \pm 5^\circ$ cases start to show some overall advancement on the windward side and on the far leeward side. The height at which the transition front is farthest upstream on the windward side is still farther from $z = 0$ and is slightly more pronounced for the $\alpha = -5^\circ$ case. The advancement on the windward side is larger from $\alpha = \pm 5^\circ$ to $\alpha = \pm 7.5^\circ$, with the most upstream portion of the wedge reaching a point that is roughly 150 mm farther upstream for $\alpha = \pm 7.5^\circ$. The peak is now trending toward $z = 0$. The development of a lesser wedge on the leeward side is also observed. Both the windward and leeward wedges continue to grow for $\alpha = \pm 10^\circ$. Note that the transition front in the region between the influence of the two wedges is roughly constant for all angles of incidence.

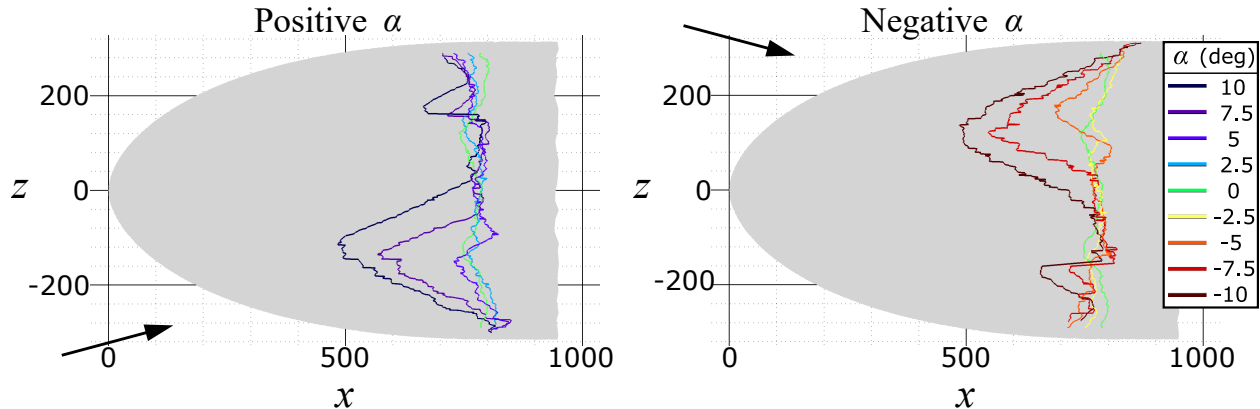


Figure 11. Transition fronts on the port side of the fuselage nose for positive (left) and negative (right) angles of incidence.

C. Comparison between IR and surface pressure

The comparison of transition fronts on the wings from estimates using IR thermography and static pressure are shown in Fig. 12. The pressure-based estimates are for $\alpha = -2^\circ$ to $\alpha = 8^\circ$, where the transition front is mostly straight across the span and is observed in the IR to advance fairly uniformly with increasing angle of incidence. All pressure ports are shown in Fig. 12 as blue circles, but only the four chordwise rows between $y = \pm 482.6$ mm and $y = \pm 1295$ mm were considered on each wing. Therefore, the pressure estimations are bounded by these coordinates. The transition fronts based on the IR thermography and the surface pressure are shown in the same color for a given angle of incidence, but the pressure-based estimations are represented as dashed line segments between rows of ports. Note that the agreement is strong between these two diagnostic methods. It is especially remarkable considering the limited spatial resolution of the pressure taps.

D. Stationary crossflow vortices at $\alpha = -5^\circ$

The stationary CF vortices leading into the transition front are examined for the $\alpha = -5^\circ$ case previously discussed and shown in Fig. 3. Figure 13(a) shows an enhanced IR image of the port wing. This image was obtained by normalizing a raw $\alpha = -5^\circ$ image by the Gaussian blur of that same image. The CF vortices are most pronounced outboard, from the wing break to near the wing tip. Note that an unfortunate outcome of enhancing the image is increased camera noise, which appears as vertical lines that exist throughout the image but are most noticeable in the large turbulent area near the root. Also unfortunate, is that the spacing of the vertical line noise is similar to the wavelength of the CF vortices; therefore, the CF vortices can only be evaluated after mitigating the camera noise.

A feature of the noise is that it is comparable between different points in the same run. As a result, the vertical lines were essentially removed by normalizing the Gaussian-blurred $\alpha = -5^\circ$ image by a similarly Gaussian-blurred $\alpha = 0^\circ$ image. The $\alpha = 0^\circ$ case was chosen for normalization because CF vortices do not appear at that condition. The upstream half of the wing is laminar, so there are no distracting features to hinder the appearance of the $\alpha = -5^\circ$ CF vortices. Therefore, the resulting image had minimal vertical line noise, and the upstream portion of the wing was

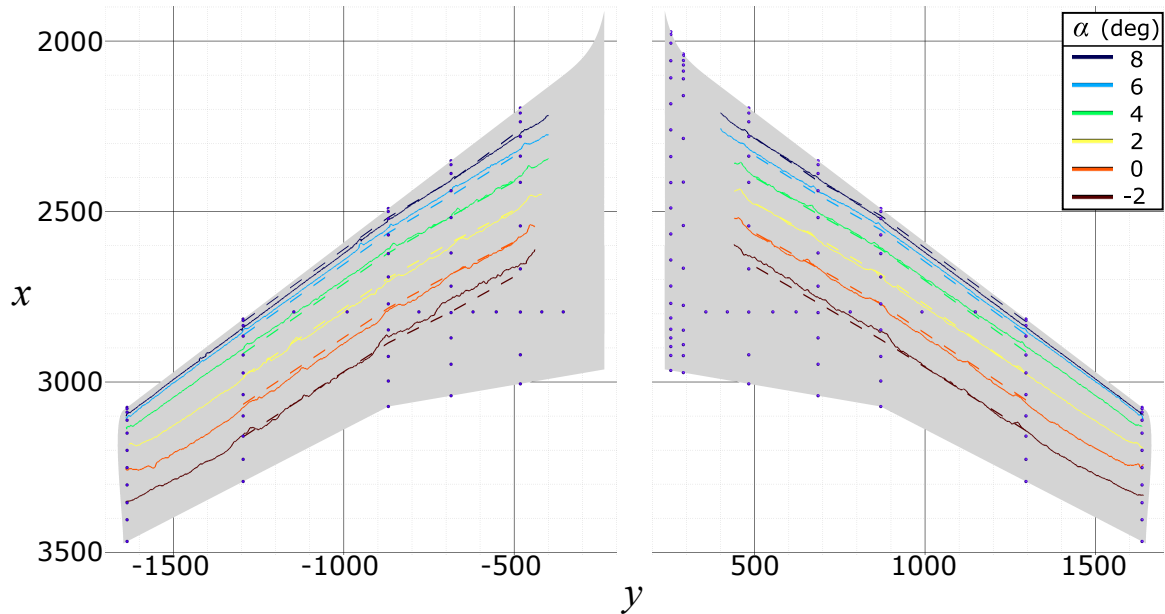


Figure 12. Comparison of transition front locations on both wings estimated from IR thermography and surface pressure: solid lines = IR, dashed lines = pressure, blue dots = pressure orifices. Angles of incidence between $\alpha = -2^\circ$ and $\alpha = 8^\circ$ are shown.

largely unaffected aside from clipping of the leading edge as a consequence of different fields of view between the two α cases.

The resulting image, transformed into body-fixed coordinates, is shown in Fig. 13(b). The transition front appears farther upstream in this image due to the field-of-view clipping from the normalization, but there is still room to evaluate the CF vortices outboard of the wing break. The secondary downstream “transition” front in the image is a relic of the $\alpha = 0^\circ$ transition front and should be ignored. The three regions selected to evaluate the CF vortices are shown in the semitransparent colored boxes in Fig. 13(b). The vortices are almost perfectly aligned with the freestream, with some slight fanning toward the wingtips further out on the span.

A representative power spectral density (PSD) was obtained for each boxed region, and those are shown in Fig. 13(c). The spectra were computed by first rotating the image in Fig. 13(b) by 37.3° to level the leading edge and allow for horizontal slices within the boxes, where each slice contains points that are approximately the same distance from the leading edge. A PSD was obtained for each 200-mm slice across the width of the box, and those PSDs were averaged over the 35-mm box depth. The wavelength from the resulting spectra was multiplied by $\cos(37.3^\circ)$ to obtain the wavelength of the CF vortices with respect to the assumed streamwise-directed streaks observed in Fig. 13(b). The spectra from all three boxed regions demonstrate a couple of peaks, where the first peak is centered on a wavelength of roughly 9–10 mm, and the second peak is between 14–16 mm and, therefore, not a harmonic. The double peak is not particularly surprising as the CF streaks visually appear uneven, with some being wider and spaced farther apart than others. The wavelength of the peaks varies slightly with sample positioning. Box 1, located near the leading edge and farther inboard, produces peaks that extend to slightly longer wavelengths. The downstream Box 3 gives a spectrum that is higher in magnitude than that from the upstream Box 2, demonstrating that the vortices grow in intensity farther downstream. The spectra on the starboard wing for mirrored box positions were also examined but not shown here to maintain clarity on the figure. The starboard spectra are also double peaked, with the peaks occurring at roughly the same wavelengths.

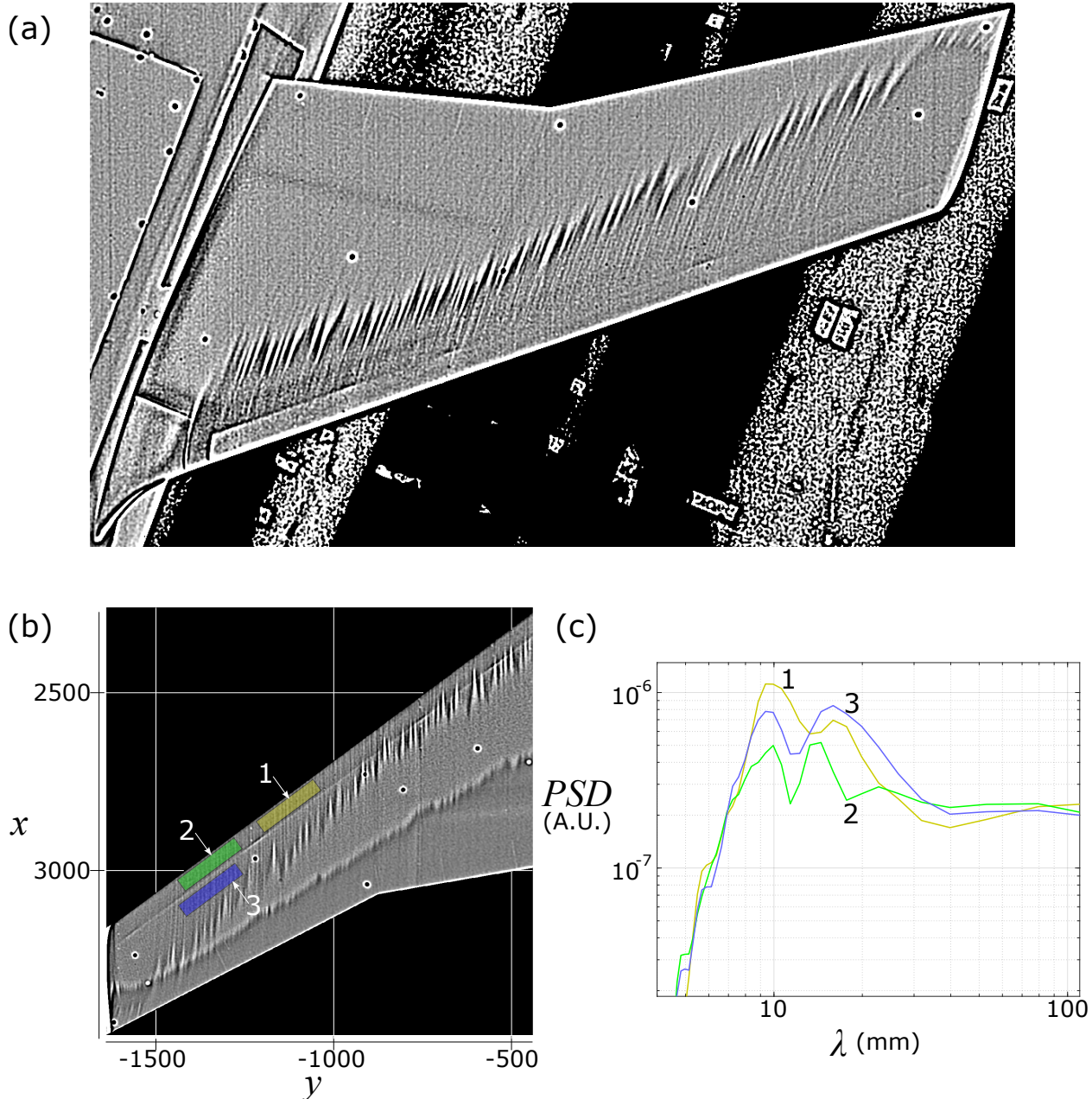


Figure 13. The evaluation of stationary crossflow vortices leading into the transition front for $\alpha = -5^\circ$. (a) Image produced from a raw $\alpha = -5^\circ$ image normalized by its own Gaussian blur. (b) Image produced from the $\alpha = -5^\circ$ -Gaussian-blur-normalized image, subsequently normalized by an $\alpha = 0^\circ$ -Gaussian-blur-normalized image, and then transformed into body-fixed coordinates. (c) Power spectral density functions obtained from evaluating the boxed regions in (b). “A.U.” refers to “arbitrary units”.

VI. Numerical Results

In this section, results from the stability analysis at select angles of incidence are first presented. These results are used to calibrate the dual N -factor criterion and to compare the resulting predictions for the transition front with the experimental measurements. Next, results from computations using select RANS-based transition models are shown, including a brief discussion of the influence of the R_q parameter used in the LM2015 model.

A. Stability analysis

The mean flow solutions used for stability analysis at the desired flow conditions were obtained using the SA RANS model. A transition front was arbitrarily imposed on the wings to maximize the flow extent, while avoiding any flow separation. Under these settings, the boundary layer is forced to remain laminar until the specified transition location. The stability analysis results are reported herein for 0° , -2.5° , -5.0° , and -7.5° angles of incidence. These results were obtained by using PSE from the attachment line up to the imposed transition front location for a total of 32 streamlines across the wing span. These are the same conditions as those of the pretest computations reported in Venkatachari et al.,¹⁰ but now the stability computations are examined in the light of experimental transition fronts and are used to determine the dual N -factor criterion. This criterion can later be applied to make predictions for other flow conditions and similar configurations. Additional angles of incidence were also studied and will be reported in a future work under preparation, along with the analysis of the instability characteristics of the fuselage.

Figures 14(a) and 14(b) show the contours of N_{CF} and N_{TS} , respectively, within the laminar region for $\alpha = 0^\circ$ on the surface of the wing, along with the transition front on the port wing as measured using IR thermography. All experimental comparisons in this section will be limited to the transition front on the port wing to maintain clarity within the figures. It is evident that the transition front closely follows the regions where N_{TS} reaches values of 10 and upwards, while N_{CF} only shows a maximum of 3 on the inboard portion of the wing downstream of midchord. Therefore, the TS instability is the dominant transition mechanism for $\alpha = 0^\circ$.

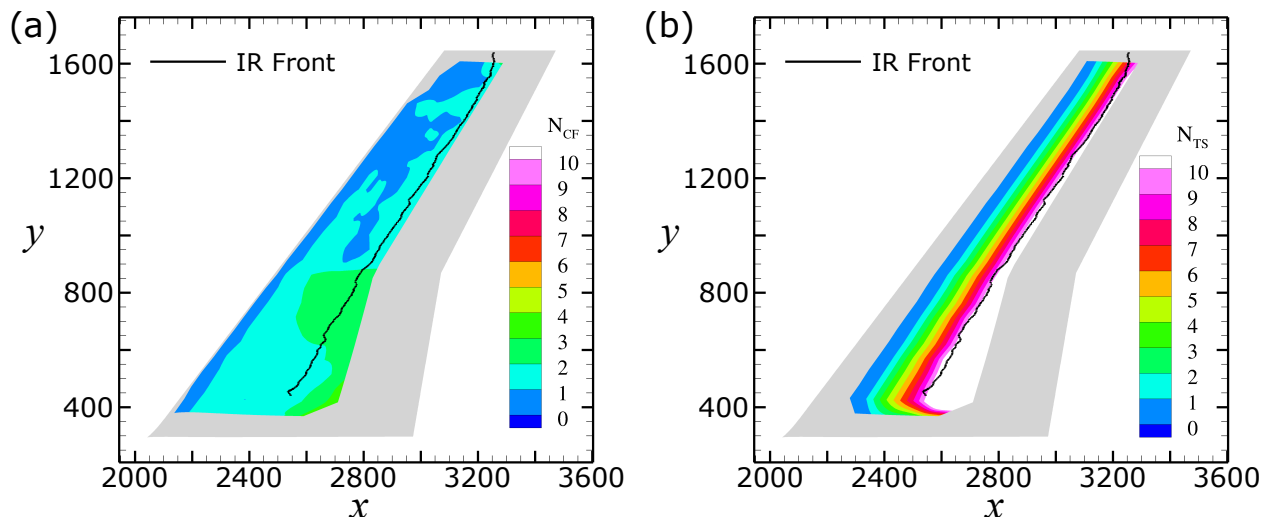


Figure 14. N -factor contours of (a) stationary CF waves ($f = 0$) and (b) TS waves ($\beta = 0$) calculated with nonorthogonal PSE for $\alpha = 0^\circ$.

As the angle of incidence decreases to -5° , it can be inferred from Fig. 15 that stationary CF has more of an influence on the transition front over the entire region inboard of the break ($5 < N_{CF} < 6$), with N_{TS} being less than 2. In the region $y \in [900, 1500]$ mm, outboard of the break, N -factors for both TS and CF instability are at significant levels indicating potential for considerable interaction between the two instability mechanisms. Only near the wingtip does N_{TS} grow significantly larger than N_{CF} .

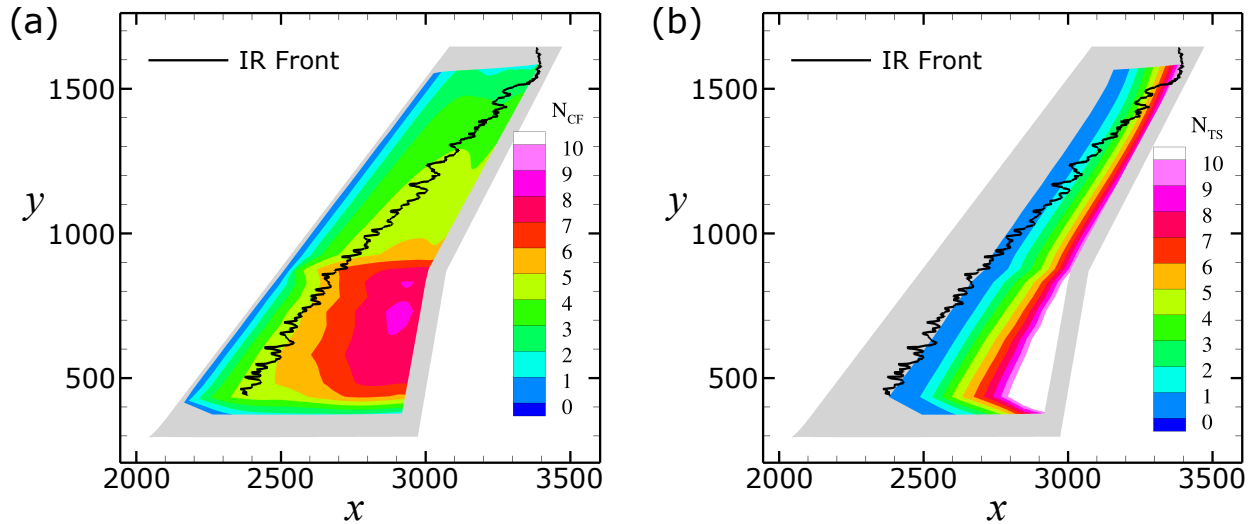


Figure 15. N -factor contours of (a) stationary CF waves ($f = 0$) and (b) TS waves ($\beta = 0$) calculated with nonorthogonal PSE for $\alpha = -5^\circ$.

Given that the two conditions $\alpha = 0^\circ$ and -5° cover scenarios where the flow instability is entirely dominated by TS and where there is a likely interaction between TS and CF mechanisms, it serves as a good dataset for calibrating the dual N -factor criterion. From the contours shown in Figs. 14 and 15, the pairs of N_{TS} and N_{CF} values are interpolated onto the inferred transition front, and are plotted as shown in Fig. 16. For $\alpha = 0^\circ$, the N_{TS} values along the transition front are largely independent of N_{CF} , whereas the two N -factors are seen to shift in a correlated fashion for $\alpha = -5^\circ$. From the pairs of N_{TS} and N_{CF} values, a fit can be obtained for the dual N -criterion of the form indicated in Eq. (9). Based on Fig. 16, $N_{TS,c} = 10$ and $N_{CF,c} = 4.5$ are seen to correlate with TS-dominated and CF-dominated transition scenarios, respectively, and choosing $a_{TS} = 1$ and $a_{CF} = 2.5$ leads to the dual N -factor criterion indicated by the black solid line, which nicely represents the trend in the data. The coefficients could be further optimized by using additional conditions to fill the gap in the data for $N_{TS} \in [6, 8]$ and $N_{CF} \in [2, 3]$, but the $\alpha = 0^\circ$ and -5° conditions were deemed sufficient for the purposes of this work. The new values of the various constants in Eq. (9) are significantly different than those used in the pretest computations by Venkatachari et al.¹⁰

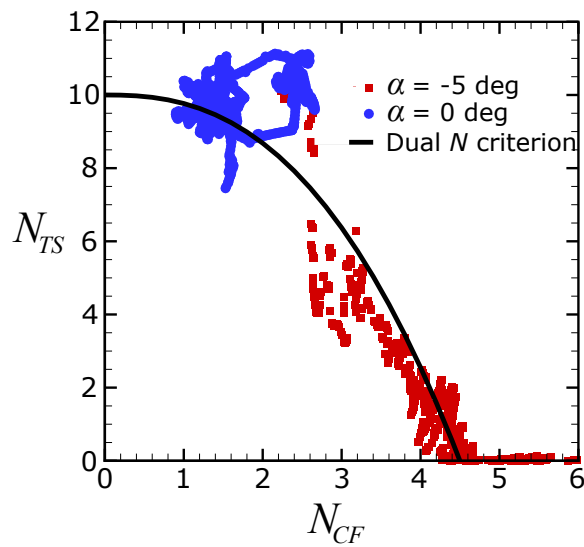


Figure 16. N -factors at experimental transition locations for stationary CF waves (N_{CF}) and TS waves (N_{TS}) calculated with nonorthogonal PSE for $\alpha = -5^\circ$ and $\alpha = 0^\circ$.

This new curve fit for the dual N -factor criterion was then applied to the previously unseen flow conditions of $\alpha = -2.5^\circ$ and -7.5° . Specifically, the transition front was determined on the basis of where the dual N -factor criterion exceeds the critical threshold of unity as shown in Fig. 17. The transition fronts from the experiment are also included for comparison.

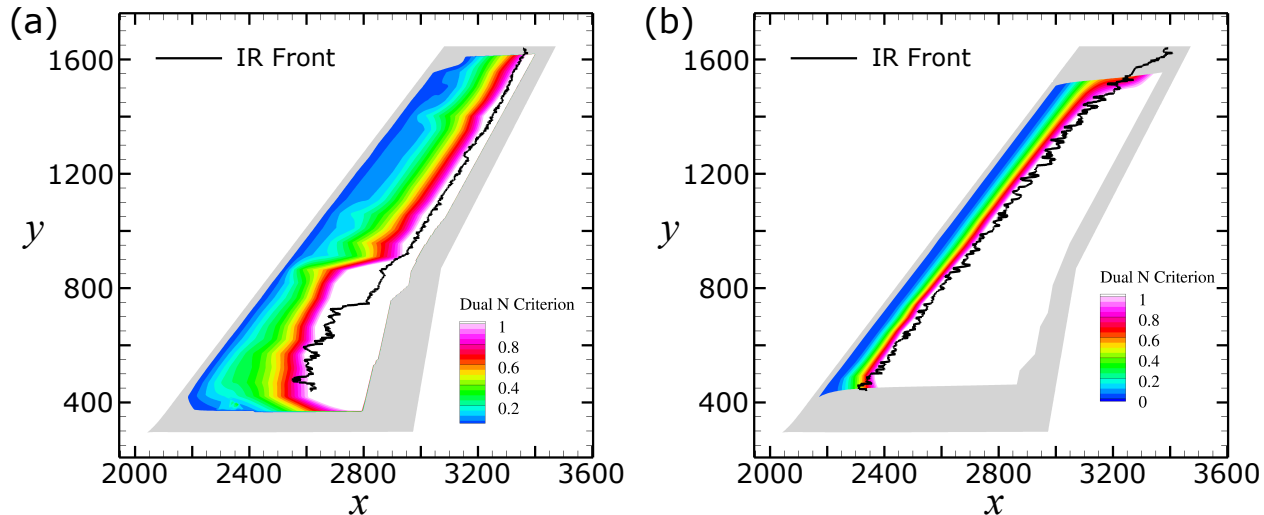


Figure 17. Computed contours of the dual $N_{TS} - N_{CF}$ criterion along with the measured transition front from IR thermography for conditions (a) $\alpha = -2.5^\circ$ and (b) $\alpha = -7.5^\circ$.

For $\alpha = -2.5^\circ$, the transition front predicted by the dual N -factor method closely matches the experimental transition front outboard of the break and also in the region $y \in [400, 700]$ mm inboard of the break. In the intermediate region of $y \in [750, 900]$ mm near the break, the front predicted by the dual N -factor is somewhat upstream of that seen during the experiment, indicating that further corrections to the curve-fit may be warranted. On the other hand, the discrepancy could also be related to the large spanwise gradients in the basic state near the break since such gradients are known to have an impact on the accuracy of the line-marching PSE computations. The CF instability becomes increasingly significant in the region inboard of the break, and that is reflected in the drastic upstream shift in the transition front seen in the experimental results as well as in the predicted front based on the dual N -factor method.

From Fig. 17(b), the predicted front from the dual N -factor criterion provides an excellent agreement with the front determined from the experiment for $\alpha = -7.5^\circ$. Furthermore, both the N -factor predictions and the experimental transition front indicate that the transition behavior is completely dominated by the CF mechanism at this condition. Thus, the previously discussed potential interaction between the TS and CF instability mechanisms for conditions $\alpha \leq -5^\circ$ is absent at this lower angle of incidence. The absence of TS instabilities at $\alpha = -7.5^\circ$ could also be attributed to the nearly constant streamwise pressure distribution observed at various spanwise stations for this flow condition, as was shown in Figs. 4 and 6 (lower surface) of Venkatachari et al.¹⁰ Overall, these results indicate that the dual N -factor criterion and the stability analysis correctly capture the transition behavior during the experiment. This finding was also confirmed by additional computations at other flow conditions that are not shown here.

B. RANS-based transition models

This section discusses the results obtained using RANS-based transition models. For all of the SST-based Langtry-Menter model variations used in this work, freestream turbulence intensity (FSTI) was enforced by using the option to sustain the desired FSTI level in the near field by adding source terms to the SST model, as put forth by Spalart and Rumsey.³⁵ This was done by specifying $FSTI = 0.08\%$ at the inlet, based on previous characterization of the tunnel,¹² along with $(\mu_t/\mu)_{inlet} = 1.0$.

All results are presented using contour plots of the turbulence index. The turbulence index was originally defined by Spalart³¹ and is an indicator for transition in CFD computations. The definition of the index for an SST-based model³⁶ differs from the original definition for an SA model. In an SA-based model, the turbulence index value always lies between 0 (laminar) and 1 (fully turbulent). Conversely, for SST-based transition models, the value of the modified turbulence index can be much greater than unity in the turbulent sections and can even be equal to a significant fraction of one in the laminar portions of the flowfield. This behavior was recently rectified in the work

by Carnes and Coder,³⁷ where a modified expression to determine the turbulence index in an SST-based model was outlined. This new definition of turbulence index for an SST-based model was used in the current work. Based on our limited experience with using this improved definition of the turbulence index, its behavior was found to closely mirror the skin-friction evolution and, hence, is more accurate in predicting the transition location in comparison with the earlier definition. In the present configuration, at least, the earlier definition³⁶ always predicted the transition front to be upstream of the location determined from the evolution of the skin-friction coefficient.

1. Influence of Transition Models

The reliability of the various LM-based transition models was evaluated in the context of the Juncture-Flow Model via computations for $\alpha = 0^\circ, -2^\circ, -2.5^\circ, -4^\circ, -5^\circ, -6^\circ$, and -7.5° . Here, the focus is on results for $\alpha = -2^\circ, -4^\circ$, and -6° . For the assessment, the LM2009 model was employed. This model accounts for TS effects alone, while two of its variants, namely the LM2015 model²⁸ and the LM-CFHE model,³⁴ both account for the combined effects of TS and stationary CF. The crossflow component of the LM2015 model assumes the onset of transition is caused by the amplification of stationary crossflow instabilities that are excited via surface roughness. The LM2015 model requires a specification of the RMS surface roughness, R_q , to account for stationary CF. Based on the experimental measurements on the port side of the wing, R_q was specified to be $3.13 \mu\text{m}$ for the results reported in this subsection.

At $\alpha = -2^\circ$, as shown in Fig. 18, all three transition models predict the transition front very close to that observed in the experiment. The onset of transition based on the LM2009 model is slightly downstream of the measured front. However, results from both LM2015 and LM-CFHE are in excellent agreement with those from the experiment, indicating that CF could play a role in causing the front to move upstream, even at this small negative angle of incidence.

As the angle of incidence decreases to $\alpha = -4^\circ$, the LM2009 model only correctly predicts the transition front near the wingtip, while it overpredicts the laminar extent across nearly 75% of the wing span. This behavior is indicated in Fig. 19(a). The LM2015 model results are shown in Fig. 19(b). It performs better than the LM2009 model, capturing a portion of the upstream shift of the transition front due to CF effects on the portion of the wing inboard of the break. However, even in this CF-dominated region, the predicted front is still downstream of the experiment transition front. The transition front predicted by the LM2015 model also indicates prominent spanwise oscillations inboard of the break. The cause is not known and is currently under investigation. The LM-CFHE model also leads to some waviness in the predicted transition front, but the amplitude of those oscillations is smaller, and the resulting predictions yield the best match with the transition front from the experiment across most of the wing span, as indicated by Fig. 19(c). Near the wing-fuselage juncture, the LM-CFHE model predicts a fully turbulent boundary layer, possibly due to the contamination from the turbulent fuselage boundary layer. It was not possible to obtain the transition fronts experimentally in this region. The seam at the junction of the leading edge fairing and the rest of the wing produced a turbulent wedge, preventing natural transition estimations closer to the fuselage.

With a further decrease in the angle of incidence to $\alpha = -6^\circ$, Fig. 20 shows that the LM-CFHE model once again provides an excellent match to the experiment across the entire span of the wing. The LM2009 model gives the worst prediction since the prominent transition mechanism is CF at $\alpha = -6^\circ$, and LM2009 only accounts for TS effects. Given that there is a near-zero streamwise pressure gradient on the wing surface, it logically follows that the TS-based LM2009 model predicts a significantly larger laminar extent than the models that account for CF. Similar to the $\alpha = -4^\circ$ case, the LM2015 model accounts for a portion of the upstream shift in transition due to stationary CF effects, but still overpredicts the laminar extent, in this case by almost 30% of the chord length across the majority of the wing. Once again, the reason for the wavy front in the region $y \in [500, 900] \text{ mm}$ is not clear. Despite accounting for roughness effects, which significantly influence the amplitudes of stationary CF, the transition predictions based on the LM2015 model are less accurate than those from the LM-CFHE model. This is surprising considering that the LM-CFHE model is based on local helicity alone and is thus unable to capture the roughness effects observed in a number of experiments. A possible reason behind this finding may be that the present flow configuration resembles the cases used to calibrate the LM-CFHE model, but may be somewhat different from the infinite-swept wing configuration used in the Arizona State University experiments³⁸ that formed the primary basis for the calibration of the LM2015 model. The LM2015 model would likely benefit from further refinement using a broader suite of transition data. To gain further insights into the shortcomings of the LM2015 model, the next subsection will investigate the influence of the RMS roughness height on the predicted transition front.

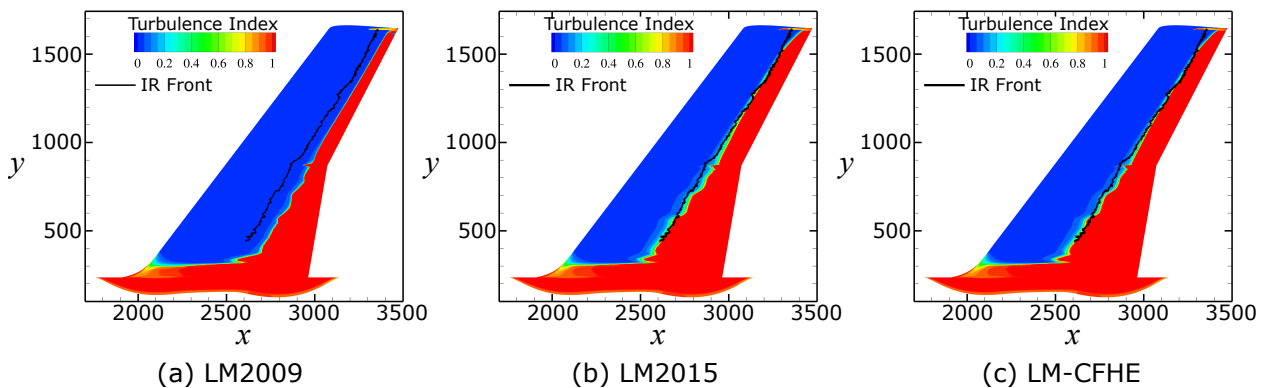


Figure 18. Predicted transition behavior as depicted via turbulence index contours for $\alpha = -2^\circ$ obtained using different transition models.

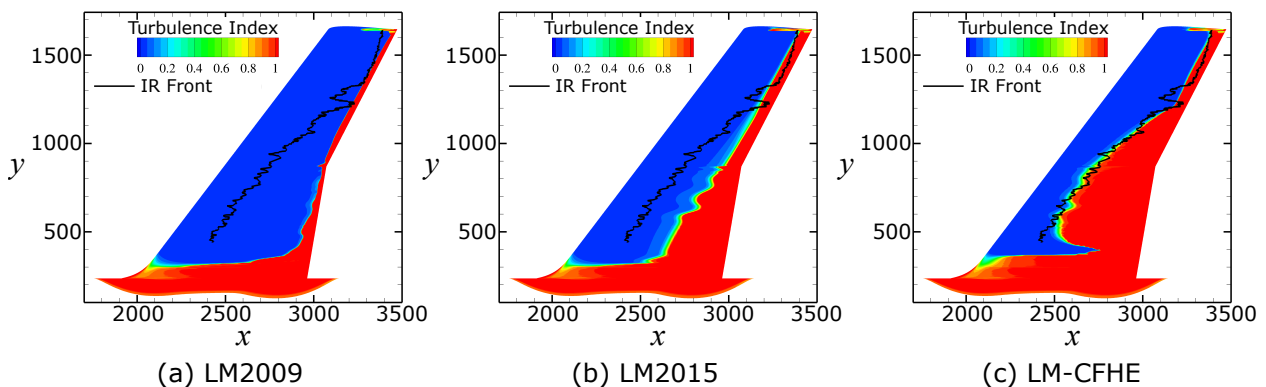


Figure 19. Predicted transition behavior as depicted via turbulence index contours for $\alpha = -4^\circ$ obtained using different transition models.

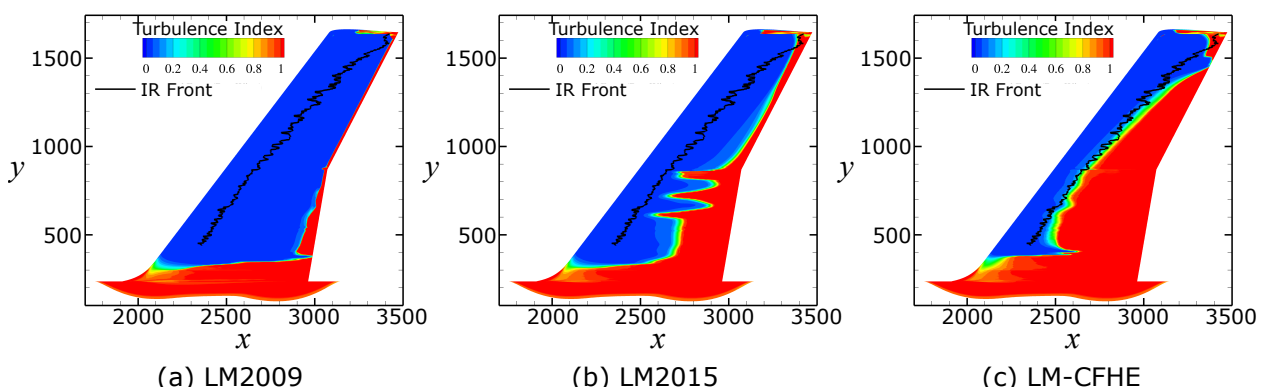


Figure 20. Predicted transition behavior as depicted via turbulence index contours for $\alpha = -6^\circ$ obtained using different transition models.

2. Influence of R_a on LM2015

As mentioned in the previous section, the LM2015 model utilizes the RMS surface roughness height to characterize the resulting impact on the transition front associated with stationary CF, yet this model performed poorly in correctly predicting the transition front on the Juncture-Flow Model. A potential explanation for this finding could be the limited data that were used in the original calibration of the model. Also, there was considerable variation in the R_q values obtained from the individual scans on the wings. As a consequence, it could be that using a single roughness level

value (R_q) may not be the most appropriate way to get the correct prediction from this transition model. Therefore, higher levels of roughness above the RMS value are considered to ascertain if the predictions improve.

Four different roughness levels, namely $R_q = 3.13 \mu\text{m}$, $4.40 \mu\text{m}$, $7.50 \mu\text{m}$, and $12.0 \mu\text{m}$, are considered for $\alpha = -5^\circ$. While the first three values are within the range of measurement data, the highest value of $12.0 \mu\text{m}$ is arbitrary and significantly higher than even the single-scan maximum R_q of $9.19 \mu\text{m}$ measured on the port wing. The results obtained by using each of these values as an input to the LM2015 model are shown in Fig. 21. The plotted results indicate that with the increase in specified roughness level, the predicted transition front from the model inches closer to that from the experiment in the region inboard of the break, where significant CF effects are expected, but it still remains significantly downstream of the measured front in the outboard region.

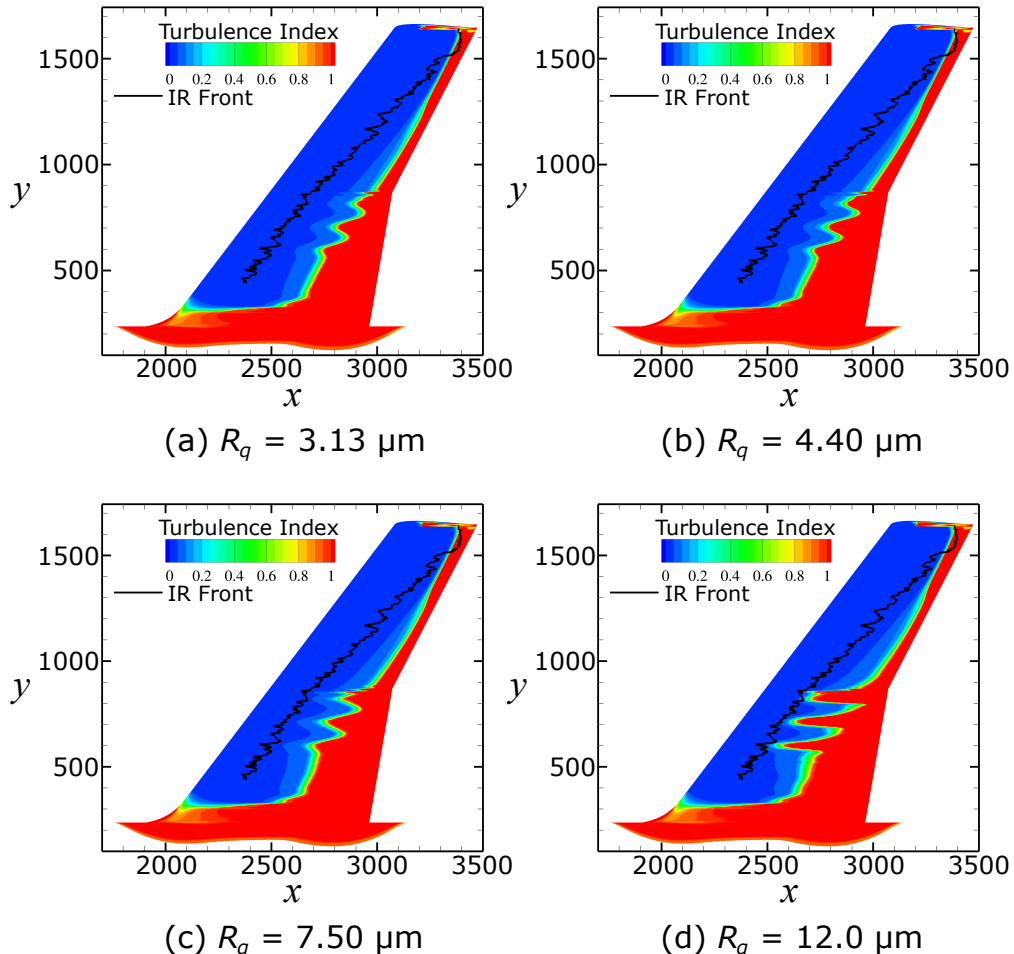


Figure 21. Influence of roughness parameter, R_q , on the LM2015 transition model in predicting transition for $\alpha = -5^\circ$, as depicted via turbulence index contours.

VII. Discussion

Although a detailed stability analysis was presented in the previous work by Venkatachari et al.,¹⁰ the results were revisited due the availability of transition front data from the experiment. The measured front was used to recalibrate the dual N -factor method that accounts for the linear amplification of Tollmien-Schlichting (TS) waves and stationary crossflow (CF) waves. The predictions with the recalibrated dual N -factor method was found to provide an excellent match to the transition front inferred from the experiment. This allows for the possibility of using the recalibrated dual N -factor method in predicting transition for other similar configurations.

Three different variants of the LM transition model were evaluated for adequate performance in regions involving significant TS and CF interaction that were found to occur for $\alpha < -2^\circ$. As expected, the LM2009 model, which

accounts only for TS-effects, performed poorly whenever crossflow effects were significant. The local helicity-based LM-CFHE model gave the most accurate predictions, closely matching the experimentally visualized transition front at the conditions investigated in the computations thus far. On the other hand, even though the LM2015 model accounts for stationary CF effects by taking into consideration the roughness level of the wing surface, and includes an additional aspect of CF transition that is not included in the LM-CFHE model, it always predicted a larger laminar extent at the conditions examined in the computational study. Inputting a higher R_q did shift the transition front upstream but the predicted shift was not sufficient to match the experiment.

A couple reasons for the poor performance of the LM2015 model could be that the roughness distribution is not homogeneous across the span and that effects of surface roughness cannot be captured by a single parameter in the form of rms height. However, even large variations in the roughness height parameter did not lead to significant improvements in this case, suggesting that the original calibration of the CF model,²⁸ which was based on a rather sparse database, does not generalize well to the present experiment. Future work includes extending the computational study by further investigating the potential sensitivity to the freestream turbulence level. Additional experiments involving combined TS and CF effects would also add considerable value toward the development of more accurate and reliable transition models for swept-wing aircraft.

The important take away from this exercise is that this new experimental dataset serves as an excellent test case to assess the performance of RANS-based transition models, especially the cases that trigger significant growth of both TS and CF instabilities. These data may also help improve the models since cases are included that involve significant growth and potential interaction between the two instability mechanisms.

VIII. Conclusions

Boundary-layer transition was measured using IR thermography on the upper surface of symmetric-airfoil wings of the NASA Juncture-Flow Model. The model was tested at angles of incidence ranging from -10° to 10° in the 14- by 22-Foot Subsonic Tunnel. The natural transition front was also identified on the port side of the fuselage and was found to be far upstream of the wings for all angles of incidence. The computational pretest analysis was helpful in identifying the overarching trends observed in the experiment, namely that the TS instability was the transition mechanism on the wings for positive angles of incidence and that stationary CF played an increasing role at negative angles of incidence. The influence of the CF instability on the transition front, observed as turbulent wedges, originated on the inboard portion of the wings around $\alpha = -2^\circ$ and progressed outboard for increasingly negative angles of incidence. The static pressure measurements were also used to determine the transition front on the wings. Despite less-than-ideal spatial resolution, the pressure-determined transition fronts showed strong agreement with the IR thermography for $\alpha \geq -2^\circ$, where the transition front is somewhat linear across the span due to the dominance of the TS instability.

Additional computations were performed based on the experimental test matrix. The transition analysis was performed via two different approaches involving the NASA OVERFLOW 2.3b CFD solver and the LASTRAC stability solver, namely, (i) LASTRAC based PSE marching along the streamline based on a partially laminar basic state obtained from OVERFLOW 2.3b by using the SA turbulence model along with an imposed transition front; and (ii) the RANS-based SST-2003-LM2009/LM2015/LM-CFHE models within OVERFLOW 2.3b. The dual N-factor model was recalibrated to predict the transition front for conditions influenced by the combination of TS and CF instabilities, and strong agreement was shown for the $\alpha = -2.5^\circ$ case. The model also proved to be effective at predicting transition when a single mechanism was prominent over the full span. The RANS-based models were generally not as strong at determining the transition front since they were formulated using data from other experiments or do not include a direct account of the underlying physics. Yet, the same general trends were demonstrated in the models where CF was considered, i.e., LM2015 and LM-CFHE. Specifically, the LM2015 code showed transition advancement on the inboard portion of the wing for small negative angles of incidence. However, the front did not advance as far upstream as observed in the experiment, even when the roughness height was artificially exaggerated within the turbulence model. The LM-CFHE model, on the other hand, does not have a roughness height input but predicted the CF-dominated transition front more accurately for this particular experiment.

Other measurements taken during this campaign, but not reported herein, include geometric scans of the model position within the tunnel, tunnel-wall pressure-rake measurements, tunnel-wall static-pressure measurements, and photogrammetry of wing deflections. Those measurements, combined with the freestream turbulence levels, the model surface roughness spectra, the model static pressures, and the transition fronts determined using IR thermography at many angles of incidence, make this dataset attractive for calibrating transition models in the future. The lessons learned from this campaign will also guide preparation for a subsequent boundary-layer transition experiment planned

in the same facility.

Acknowledgements

This work was supported by the NASA Transformational Tools and Technologies project of the Transformative Aeronautics Concepts Program. The authors thank all members of the Juncture-Flow Team for their dedication and insights throughout the course of this effort. The authors would also like to thank the staff of the 14- by 22-Foot Subsonic Tunnel for their support during the test entry. The research of the last two authors is funded through the National Institute of Aerospace (NIA) under the cooperative agreement 2A00 (Activity 201133). The computational resources supporting this work were provided by the K cluster at NASA Langley Research Center and by the NASA High-End Computing (HEC) Program through the NASA Advanced Supercomputing (NAS) Division at the Ames Research Center.

References

- ¹Taylor, N. J. and Rumsey, C. L., “CFD Validation Experiments: Toward a Broader Perspective,” AIAA Paper 2021-1933, January 2021.
- ²Rumsey, C. L., Ahmad, N. N., Carlson, J. R., Kegerise, M. A., Neuhart, D. H., Hannon, J. A., Jenkins, L. N., Yao, C. S., Balakumar, P., Bartram, S. M., Pulliam, T. H., Olsen, M. E., and Spalart, P. R., “CFD Comparisons with Updated NASA Juncture Flow Data,” AIAA Paper 2021-1427, January 2021.
- ³Kegerise, M. A., Neuhart, D. H., Hannon, J. A., and Rumsey, C. L., “An Experimental Investigation of a Wing-Fuselage Junction Model in the NASA Langley 14- by 22-Foot Subsonic Wind Tunnel,” AIAA Paper 2019-0077, January 2019.
- ⁴Kegerise, M. A. and Neuhart, D. H., “An Experimental Investigation of a Wing-Fuselage Junction Model in the NASA Langley 14- by 22-Foot Subsonic Tunnel,” NASA TM 2019-220286, June 2019.
- ⁵Jenkins, L. N., Yao, C. S., and Bartram, S. M., “Flow-Field Measurements in a Wing-Fuselage Junction Using an Embedded Particle Image Velocimetry System,” AIAA Paper 2019-0078, January 2019.
- ⁶Rumsey, C. L., “NASA Langley Turbulence Modeling Resource Website,” <https://turbmodels.larc.nasa.gov>.
- ⁷Kegerise, M. A., Leidy, A. N., Hannon, J. A., Rumsey, C. L., and Pulliam, T. H., “Measurements and Computations of the Turbulent Corner Flow on the NASA Juncture-Flow Model with a Symmetric Wing,” AIAA Paper 2023-xxxx, January 2023.
- ⁸Quast, A., “Detection of Transition by Infrared Image Technique,” *12th International Congress on Instrumentation in Aerospace Simulation Facilities*, Williamsburg, VA, 1987, pp. 125–134.
- ⁹Carlomango, G. M. and Cardone, G., “Infrared Thermography for Convective Heat Transfer Measurements,” *Experiments in Fluids*, Vol. 49, 2010, pp. 1187–1218.
- ¹⁰Venkatachari, B. S., Paredes, P., Choudhari, M. M., Li, F., and Chang, C.-L., “Pretest Computational Assessment of Boundary Layer Transition in the NASA Juncture Flow Model with an NACA 0015-Based Wing,” AIAA Paper 2021-2502, July 2021.
- ¹¹Dagenhart, J. R. and Saric, W. S., “Crossflow Stability and Transition Experiments in Swept-Wing Flow,” NASA TP 1999-209344, July 1999.
- ¹²Neuhart, D. H. and McGinley, C. B., “Free-Stream Turbulence Intensity in the Langley 14- by 22-Foot Subsonic Tunnel,” NASA TP 213247, 2004.
- ¹³Gentry, G. L., Quinto, F. P., Gatlin, G. G., and Applin, Z. T., “The Langley 14- by 22-Foot Subsonic Tunnel,” NASA TP 3008, 1990.
- ¹⁴Leidy, A. N., “Roughness Measurements on the Symmetric-Airfoil Wings of the NASA Juncture-Flow Model,” NASA TM 2023-xxxxxx, xx 2023.
- ¹⁵Nichols, H. and Buning, P. G., “User’s Manual for OVERFLOW 2.3,” <https://overflow.larc.nasa.gov/home/users-manual-for-overflow-2-3/>, August 2019.
- ¹⁶Roe, P. L., “Approximate Riemann Solvers, Parameter Vectors, and Difference Schemes,” *Journal of Computational Physics*, Vol. 43, No. 2, 1981, pp. 357–372.
- ¹⁷Nichols, R. H., Tramel, R. W., and Buning, P. G., “Solver and Turbulence Model Upgrades to OVERFLOW 2 for Unsteady and High-Speed Applications,” AIAA Paper 2006-2824, June 2006.
- ¹⁸Chang, C.-L., “LASTRAC.3d: Transition Prediction in 3D Boundary Layers,” AIAA Paper 2004-2542, June 2004.
- ¹⁹Herbert, T., “Parabolized Stability Equations,” *Annual Review of Fluid Mechanics*, Vol. 29, No. 1, 1997, pp. 245–283.
- ²⁰Chang, C.-L., “Langley Stability and Transition Analysis Code (LASTRAC) Version 1.2 User Manual,” NASA TM 2004-213233, June 2004.
- ²¹Horstmann, K. H., Redeker, G., Quast, A., Dressler, U., and Bieler, H., “Flight Test With a Natural Laminar Flow Glove on a Transport Aircraft,” AIAA Paper 1990-3044, August 1990.
- ²²Arnal, D., “Boundary Layer Transition: Prediction Based on Linear Theory,” *Special Course on Progress in Transition Modeling*. AGARD-R-793, April 1994, pp. 1–62.
- ²³Schrauf, G., Perraud, J., Vitiello, D., and Lam, F., “Comparison of Boundary-Layer Transition Predictions Using Flight Test Data,” *Journal of Aircraft*, Vol. 35, No. 6, 1998, pp. 891–897.
- ²⁴Menter, F. R., Langtry, R. B., and Völker, S., “Transition Modelling for General Purpose CFD Codes,” *Flow, Turbulence and Combustion*, Vol. 77, 2006, pp. 277–303.
- ²⁵Langtry, R. B. and Menter, F. R., “Correlation-Based Transition Modeling for Unstructured Parallelized Computational Fluid Dynamics Codes,” *AIAA Journal*, Vol. 47, No. 12, 2009, pp. 2894–2906.
- ²⁶Menter, F. R., “Two-Equation Eddy-Viscosity Turbulence Models for Engineering Applications,” *AIAA Journal*, Vol. 32, No. 8, 1994, pp. 1598–1605.

- ²⁷Menter, F. R., Kuntz, M., and Langtry, R. B., "Ten Years of Industrial Experience with the SST Turbulence Model," *Turbulence, Heat and Mass Transfer*, Vol. 4, No. 1, 2003, pp. 625–632.
- ²⁸Langtry, R. B., Sengupta, K., Yeh, D. T., and Dorgan, A. J., "Extending the Local $\gamma - Re_{\theta t}$ Correlation based Transition Model for Crossflow Effects," AIAA Paper 2015-2474, June 2015.
- ²⁹Coder, J. G. and Maughmer, M. D., "Computational Fluid Dynamics Compatible Transition Modeling Using an Amplification Factor Transport Equation," *AIAA Journal*, Vol. 52, No. 11, 2014, pp. 2506–2512.
- ³⁰Coder, J. G., Pulliam, T. H., and Jensen, J. C., "Contributions to HiLiftPW-3 Using Structured, Overset Grid Methods," AIAA Paper 2018-1039, January 2018.
- ³¹Spalart, P. R. and Allmaras, S. R., "A One-Equation Turbulence Model for Aerodynamic Flows," *Recherche Aerospaciale*, Vol. 1, 1994, pp. 5–21.
- ³²Medida, S. and Baeder, J. D., "Application of the Correlation-based $\gamma - Re_{\theta t}$ Transition Model to the Spalart-Allmaras Turbulence Model," AIAA Paper 2011-3979, June 2011.
- ³³Medida, S., *Correlation-based Transition Modeling for External Aerodynamic Flows*, Ph.D. thesis, University of Maryland, 2014.
- ³⁴Grabe, C., Nie, S., and Krumbein, A., "Transport Modeling for the Prediction of Crossflow Transition," *AIAA Journal*, Vol. 56, No. 8, 2018, pp. 3167–3178.
- ³⁵Spalart, P. R. and Rumsey, C. L., "Effective Inflow Conditions for Turbulence Models in Aerodynamic Calculations," *AIAA Journal*, Vol. 45, No. 10, 2007, pp. 2544–2553.
- ³⁶Sclafani, A., Slotnick, J., Vassberg, J., and Pulliam, T., "Extended OVERFLOW Analysis of the NASA Trap Wing Wind Tunnel Model," AIAA Paper 2012-2919, June 2012.
- ³⁷Carnes, J. A. and Coder, J. G., "Analyzing the Near-Wall Behavior of the Langtry-Menter Transition Model," *Flow, Turbulence and Combustion*, Vol. 108, No. 3, 2022, pp. 683–715.
- ³⁸Rade茨sky, R. H., Reibert, M. S., Saric, W. S., and Takagi, S., "Effect of Micron-Sized Roughness on Transition in Swept-Wing Flows," AIAA Paper 1993-0076, January 1993.